Research Square

Preprints are preliminary reports that have not undergone peer review.
They should not be considered conclusive, used to inform clinical practice,
or referenced by the media as validated information.

Mitigating Liquefaction-Induced Manhole Uplift with a Surface-Installed Weight Collar: Exploratory Shaking Table Tests and Implications for Post-Earthquake Road and Sewer Functionality

Khin Nyein Chan Kyaw
Shibaura Institute of Technology
Daiki Fujita
Shibaura Institute of Technology
Shinya Inazumi
inazumi@shibaura-it.ac.jp

Shibaura Institute of Technology

Research Article

Keywords: liquefaction, manhole uplift, earthquake disaster mitigation, lifeline resilience, sewerage infrastructure, emergency road access, weighting retrofit, shaking table test, limit equilibrium analysis

Posted Date: November 27th, 2026

DOI: https://doi.org/10.21203/rs.3.rs-11763832/v1

License: This work is licensed under a Creative Commons Attribution 4.0 International License.
Read Full License

Additional Declarations: No competing interests reported.

TITLE

Mitigating Liquefaction-Induced Manhole Uplift with a Surface-Installed Weight Collar: Exploratory Shaking Table Tests and Implications for Post-Earthquake Road and Sewer Functionality

AUTHORS' INFORMATION

Khin Nyein Chan Kyaw [1], Daiki Fujita [2] and Shinya Inazumi [3,*]

[1] Graduate student, Graduate School of Engineering and Science, Shibaura Institute of Technology, Tokyo 135-8548, Japan; na24503@shibaura-it.ac.jp
[2] Graduate student, Graduate School of Engineering and Science, Shibaura Institute of Technology, Tokyo 135-8548, Japan; ah22066@shibaura-it.ac.jp
[3] Ph.D., Professor, College of Engineering, Shibaura Institute of Technology, Tokyo 135-8548, Japan; inazumi@shibaura-it.ac.jp
[*] Corresponding author

ABSTRACT

Background Liquefaction-induced uplift of sewer manholes is a recurrent form of earthquake damage to urban lifelines. Uplifted manholes obstruct roads needed for evacuation and emergency response, and damaged manholes interrupt wastewater service during recovery. Because manholes are numerous and lie beneath roads in service, pre-earthquake countermeasures must be quick to install with limited excavation. This study examines a retrofit in which a weight collar of precast rings and mortar is installed from the road surface around the top 425 mm of an existing manhole.

Results Paired 1-g shaking table tests were conducted on 1/20-scale models of a standard No. 1 manhole. The models were embedded side by side in loose, nominally saturated silica sand (relative density 38–40%) with the groundwater table at the ground surface and were shaken sinusoidally at 3 Hz with nominal amplitudes of 0.5, 1.0, and 1.5 m/s^2. The unweighted model was uplifted by 9.6–14.0 mm (8–12% of its height) after a substantial buildup of excess pore water pressure. The model with the collar showed no measurable uplift. Because the surrounding ground settled by 11–14 mm, it still protruded by an estimated 10–13 mm above the mean settled surface, about half that of the unweighted model. Because the collar changed both mass and geometry, the response cannot be attributed to the added weight alone. A limit equilibrium interpretation, conditional on a back-calculated equivalent excess pore water pressure ratio of about 0.45–0.55, gives factors of safety close to unity (0.95–1.09) for the weighted model. In an illustrative prototype calculation, three rings raised the factor of safety at full liquefaction from 0.76 to 1.09 for a groundwater table depth of 1.0 m, but only from 0.55 to 0.72 when the collar was submerged.

Conclusions The tests provide exploratory evidence that a surface-installed weight collar can suppress one damage mode, absolute uplift, under the tested small-scale conditions. Residual protrusion, pipe connections, and groundwater conditions remain decisive for post-earthquake road and sewer functionality. A three-step screening procedure based on the consequence of failure, the seasonal high groundwater level, and the required functional performance is proposed for prioritizing retrofit sites.

KEYWORDS

liquefaction; manhole uplift; earthquake disaster mitigation; lifeline resilience; sewerage infrastructure; emergency road access; weighting retrofit; shaking table test; limit equilibrium analysis

Highlights

- Liquefaction-induced manhole uplift threatens emergency road access and wastewater service after earthquakes.
- A surface-installed weight collar suppressed measurable uplift of a model manhole in three 1-g shaking table tests, whereas the paired unweighted model was uplifted by 8–12% of its height.
- Settlement of the surrounding loose sand still left the weighted model protruding by an estimated 10–13 mm, about half the protrusion of the unweighted model.
- A back-calculated equivalent pressure ratio of about 0.5 is consistent with both responses but is not a measured value.
- In an illustrative prototype calculation, the collar retains its dead-weight contribution only above the groundwater table, which makes groundwater conditions central to site screening.

1. INTRODUCTION

1.1 Background

Liquefaction of saturated loose sand under cyclic shearing is one of the most damaging geotechnical effects of earthquakes (Seed and Idriss 1971; Ishihara 1993; Youd et al. 2001; Idriss and Boulanger 2008; Towhata 2008). When the excess pore water pressure reaches the initial effective overburden stress, the soil loses its shear strength. The liquefied soil then behaves temporarily as a dense fluid. Buildings and embankments on such ground settle and tilt. In contrast, buried structures that are lighter than the displaced soil are uplifted.

Sewer manholes are the most numerous structures of this type. A manhole is a hollow reinforced concrete shaft. Its apparent unit weight is typically 10–17 kN/m^3, whereas the unit weight of saturated sand is 18–20 kN/m^3. Manholes are installed in open-cut trenches. The trench backfill is usually sandy soil. It is often loosely compacted and frequently lies below the groundwater table.

Manhole uplift has been reported after many earthquakes. Manholes were uplifted during the 1993 Kushiro-oki earthquake (Koseki et al. 1997b). Sewer pipes were uplifted during the 1994 Sanriku-Haruka-oki earthquake (Koseki et al. 1998). About 1,400 manholes were uplifted during the 2004 Niigata-ken Chuetsu earthquake. In that event, liquefaction of the trench backfill, and not of the native clayey ground, caused the damage (Yasuda and Kiku 2006; Tobita et al. 2009). The 2011 Tohoku earthquake caused extensive liquefaction in reclaimed land around Tokyo Bay (Bhattacharya et al. 2011; Yasuda et al. 2012; Tokimatsu et al. 2012). Manholes, buried tanks, and underground parking structures were uplifted over a wide area (Tokimatsu et al. 2012; MLIT 2011; Chian and Tokimatsu 2012). Similar damage to buried pipe networks occurred during the 2010–2011 Canterbury earthquakes in New Zealand (Cubrinovski et al. 2011). Uplifted manholes were again reported after the Noto Peninsula earthquake of January 1, 2024 (Miyajima et al. 2024).

The consequences extend beyond the structure and into disaster response and recovery. An uplifted manhole protrudes above the road surface and can obstruct evacuation and emergency vehicles at the time when road access is most needed. Pipe connections are sheared or pulled apart, sewage flow is interrupted, and the loss of wastewater service prolongs the disruption of daily life in the affected area (MLIT 2011). Restoration requires excavation at each damaged manhole and competes with other recovery work for crews and equipment. Manholes are spaced at intervals of a few tens of meters along every sewer line. The number of structures that would require protection before an earthquake is therefore very large. For a pre-earthquake mitigation program, the cost, the

construction time, and the traffic disruption per manhole determine whether a retrofit can be deployed at the necessary scale.

1.2 Previous Studies on Uplift Mechanisms and Prediction

The uplift mechanism has been studied by 1-g model tests, centrifuge model tests, and numerical analysis. Koseki et al. (1997a) conducted shaking table tests on box structures and manholes. They identified three stages of behavior. The first is rapid uplift accompanied by deformation of the surrounding soil. The second is slower uplift associated with migration of pore water. The third is settlement during reconsolidation. They also evaluated a factor of safety from the vertical force equilibrium by using the measured excess pore water pressure. This factor of safety decreased to about unity at the onset of uplift. The same factor of safety is used in Japanese design practice for common utility ducts and sewerage facilities (Japan Sewage Works Association 2006; Japan Road Association 1986). It was later examined for buried pipes by centrifuge model tests (Ling et al. 2003).

The equilibrium approach predicts the onset of uplift but not the uplift displacement. Tobita et al. (2011) conducted centrifuge model tests on manholes in a liquefiable trench. The uplift displacement depended strongly on the groundwater table depth, the intensity and duration of shaking, and the apparent unit weight of the manhole. Tobita et al. (2012) then proposed a closed-form estimate of the maximum uplift displacement. In this method, the liquefied backfill is idealized as a heavy fluid. The volume of the uplifted manhole is balanced against the settlement of the backfill.

Chian and Madabhushi (2012) and Chian et al. (2014) studied circular structures by centrifuge model tests and image analysis. They observed that liquefied soil flowed from the crown toward the invert. The uplift rate was nearly constant while the soil remained liquefied. Uplift ceased when shaking stopped. For cut-and-cover tunnels, Chou et al. (2011) identified ratcheting of sand beneath the structure, pore water migration, and bottom heave as separate mechanisms. Watanabe et al. (2016) derived a simplified stability evaluation method from centrifuge model tests. Sasaki and Tamura (2004) proposed empirical equations for the uplift displacement of buried structures. Effective stress analyses have reproduced many of these observations for tunnels, large underground structures, and hollow cylinders (Kang et al. 2014; Liu and Song 2005; Azadi and Mir Mohammad Hosseini 2010; Sudevan et al. 2020). However, simulation of the post-liquefaction, large-strain stage remains difficult.

1.3 Existing Countermeasures and Their Limitations

Existing countermeasures are classified into three groups. The first group prevents liquefaction of the backfill. It includes compaction to a high degree, cement-treated or crushed-stone backfill, and recycled granular backfill (Yasuda and Kiku 2006; Kang et al. 2013; Otsubo et al. 2016b; Japan Sewage Works Association 2006). These methods are effective for new construction and for reconstruction after damage. However, the full depth of the trench must be excavated. The second group dissipates the excess pore water pressure. It includes gravel drains and drainage devices built into the manhole wall (Kang et al. 2013; Orense et al. 2003; Otsubo et al. 2016a). The third group restrains the structure mechanically, for example with cutoff walls, anchors, or helical piles (Mahmoud et al. 2020; Nokande et al. 2023).

All three groups have practical limitations for existing manholes beneath roads in service. The excavation depth increases with the manhole depth. Shoring is required. Adjacent utilities must be exposed by hand excavation. The work can rarely be completed within a single road closure. These constraints limit the rate at which existing networks can be strengthened before the next earthquake.

Increasing the weight of the structure is a simpler option. The weight appears in the numerator of the factor of safety. The apparent unit weight of the manhole is also a controlling variable in the uplift estimate of Tobita et al. (2012). A weighting retrofit that is installed entirely from the road surface has been proposed for existing manholes (Nakao et al. 2022). Nakao et al. (2022) evaluated its applicability analytically, through case studies of the factor of safety against uplift and the amount of uplift. To the authors' knowledge, its performance under liquefaction has not yet been examined experimentally in the published literature. In addition, three questions remain unanswered. The first is how much of the theoretical buoyant force is mobilized on a manhole during shaking. The second is how much of the added weight is canceled by the buoyancy of the added volume when the weight lies below the groundwater table. The third concerns functional performance. A manhole that is not uplifted may still protrude above the road surface if the surrounding ground settles, and it is this step that affects the passage of vehicles after an earthquake.

1.4 Objectives and Contributions

This study examines the weighted-ring retrofit as a pre-earthquake mitigation measure for existing sewer manholes. Exploratory model tests and a simplified analytical interpretation are used. The contributions are as follows.

(1) Paired 1-g shaking table tests compare a weighted model and an unweighted model in the same liquefiable deposit at three shaking intensities. The vertical displacement and the excess pore water pressure were measured continuously. The paired arrangement reduces the influence of test-to-test variation in ground conditions on the comparison. It does not ensure identical local density, drainage, or confinement around the two models.

(2) The limit equilibrium factor of safety used in practice is implemented in a general form. The pore water pressure is integrated over the actual geometry of the manhole and the weight collar. The hydrostatic and excess components are separated. The groundwater table depth and the excess pore water pressure ratio are explicit variables. The formulation is a transparent accounting of forces and not a new mechanical principle.

(3) The tests are back-analyzed to obtain an equivalent excess pore water pressure ratio and a phenomenological time constant of uplift. Both quantities are conditional on the assumptions of the back-analysis and are not design parameters.

(4) The calculation is applied to one prototype configuration as an illustration. Force components and a sensitivity analysis show how the number of weight rings, the groundwater table depth, and the assumed pressure profile affect the calculated factor of safety, and under which groundwater conditions the collar retains its calculated benefit.

(5) Absolute uplift is distinguished from the residual protrusion of the manhole above the settled ground surface, which governs road passability after an earthquake.

Section 2 describes the retrofit and the limit equilibrium formulation. Sections 3 and 4 present the test program and the results. Section 5 presents the analytical interpretation and the illustrative prototype-scale calculation. Section 6 discusses the mechanism, the implications for disaster mitigation and design, a screening approach for pre-earthquake retrofit, and the limitations. Section 7 summarizes the conclusions.

2. WEIGHTED-RING RETROFIT AND LIMIT EQUILIBRIUM FORMULATION

2.1 Concept and Construction Procedure

The retrofit does not prevent liquefaction. Instead, it adds dead load to the manhole. The added load keeps the sum of the weight and the frictional resistance larger than the uplift force when the surrounding soil liquefies (Fig. 1). The load is provided by a weight collar placed around the manhole neck directly below the pavement.

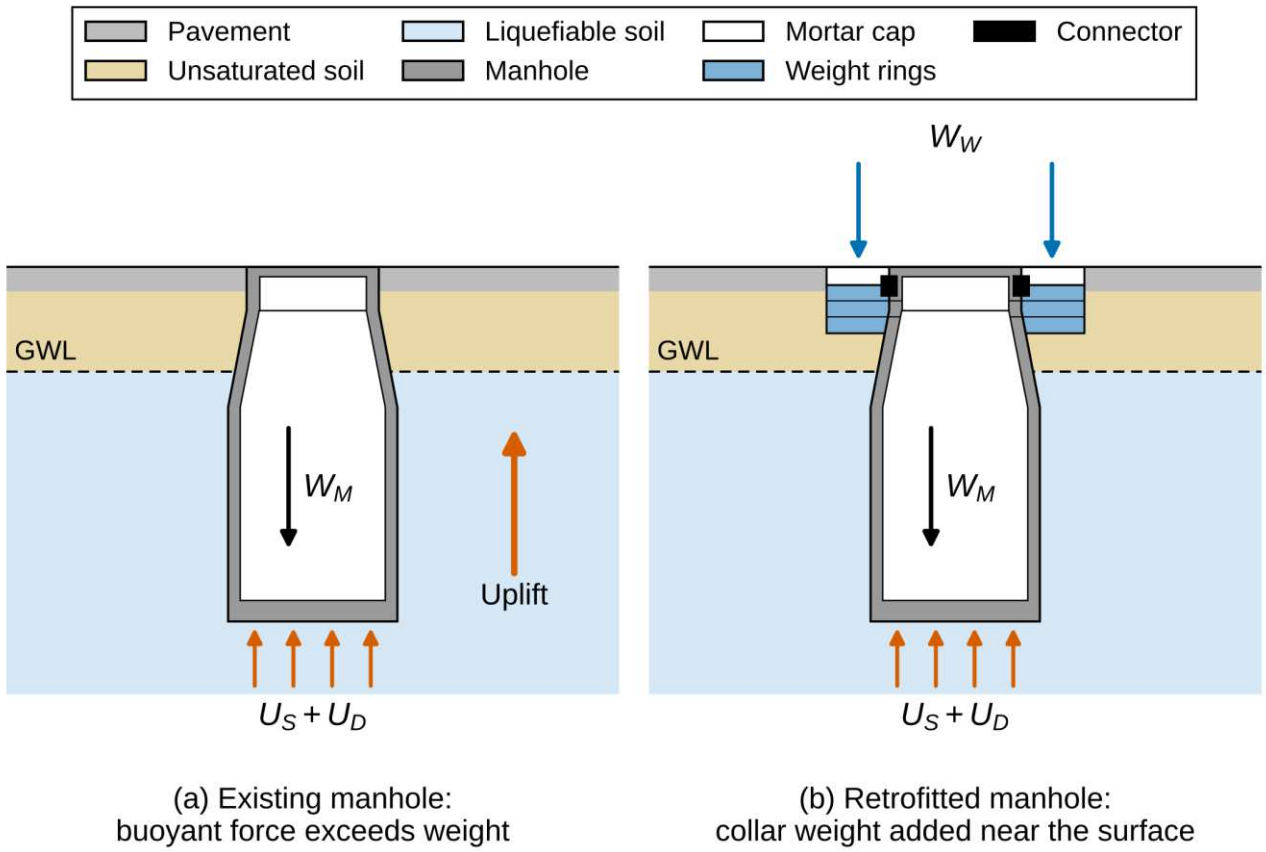

Figure 1. Concept of the weighted-ring retrofit.

Following Nakao et al. (2022), the retrofit is constructed from the road surface in six steps.

(1) The pavement and base course around the manhole cover are cut and removed over a diameter of 1.6 m. The machine normally used for adjusting manhole frames is employed.

(2) The excavation is extended to the required depth. The maximum depth is 425 mm below the road surface.

(3) One to three precast weight rings are placed around the manhole neck. Each ring is 100 mm high, with an inner diameter of 820 mm and an outer diameter of 1,600 mm.

(4) Stainless steel connectors are bolted between the cover frame and the shaft. The frame, the collar, and the shaft are then intended to act as a single body.

(5) Non-shrink mortar is cast over and around the rings and the frame to a thickness of 110 mm. The mortar cap locks the assembly and adds weight.

(6) The pavement is restored.

The unit weight is 21 kN/m^3 for the rings and 23 kN/m^3 for the mortar cap. The added weight is 7.39, 10.50, and 13.61 kN for one, two, and three rings, respectively (Nakao et al. 2022). The collar weight is assumed to be

transferred to the shaft through the connectors and the mortar cap. The structural adequacy of this load path, the design of the connection, and its durability were not assessed in this study. In the calculations below, the collar and the manhole are treated as one rigid body.

Table 1 compares the installation concept described by Nakao et al. (2022) with backfill improvement, a countermeasure commonly applied to existing manholes. The entries for the retrofit describe the intended installation and were not verified in this study. The main difference is the excavation depth. In the retrofit, the excavation is shallow and independent of the manhole depth.

Table 1. Comparison of the weighted-ring retrofit (Nakao et al. 2022) with conventional backfill improvement for existing manholes.

Item	Backfill compaction or replacement	Weighted-ring retrofit
Principle	Prevents liquefaction of the trench backfill	Adds dead load against buoyancy; liquefaction is permitted
Excavation	Full manhole depth over the trench area	Diameter of 1.6 m; depth of 425 mm or less
Shoring	Required for deep manholes	Not required for an excavation of 425 mm (Nakao et al. 2022)
Effect on adjacent utilities	Hand excavation near buried pipes and cables	No excavation below 425 mm
Quality control	Degree of compaction of 90% or more	Weight of precast units and mortar volume
Road closure	Increases with manhole depth and shoring	Installation and pavement restoration within one day (Nakao et al. 2022)
Design variable	Density or strength of backfill	Number of weight rings (1–3)
Governing limitation	Cost and construction time	Benefit decreases when the collar is submerged (Section 5.4)

2.2 Generalized Factor of Safety Against Uplift

In Japanese practice, uplift is evaluated by the ratio of the resisting forces to the uplift forces (Japan Sewage Works Association 2006; Japan Road Association 1986). The pore water pressure force is computed on the base area of the structure. For a prismatic body, this force is the complete pressure resultant. A manhole narrows through an eccentric cone to the neck, and a collar is wider than the shaft. For such a body, the base-area calculation is complete only if the soil above the inclined and horizontal surfaces is assigned consistently. In this paper, the pore water pressure is integrated over the entire wetted surface. The physical model is the same as in the conventional calculation. Only the accounting of the forces on the inclined and horizontal surfaces differs, and it becomes explicit.

Consider a manhole of height h whose top is at the ground surface. The groundwater table is at depth d_w. The soil above the groundwater table has a total unit weight γ_t. The soil below it has a saturated unit weight γ_{sat} and a buoyant unit weight $\gamma' = \gamma_{sat} - \gamma_w$. The factor of safety against uplift is

$$F_S = \frac{W_M + W_W + W_S + Q_B}{U_S + U_D} \tag{1}$$

where W_M is the weight of the manhole, W_W is the weight of the collar, and W_S is the weight of the unsaturated soil above the conical section, within the cylindrical envelope of the shaft. Q_B is the frictional resistance on the wall above the groundwater table. U_S is the hydrostatic pore water pressure force, and U_D is the excess pore water pressure force.

Below the groundwater table, the pore water pressure is the sum of two parts. The hydrostatic part is $\gamma_w(z - d_w)$. The excess part is a fraction r_u of the initial vertical effective stress, $\Delta u = r_u\, \sigma'_{v0}(z)$, where $\sigma'_{v0} = \gamma_t\, d_w + \gamma'(z - d_w)$. This distribution is referred to as profile I. It is the idealized design profile of the guidelines (Japan Sewage Works Association 2006; Japan Road Association 1986) and not a measured pressure distribution. Applying the divergence theorem to the part of the body below the groundwater table gives the two forces in closed form:

$$U_S = \gamma_w\, V(d_w) \tag{2}$$

$$U_D = r_u[\gamma_t\, d_w\, A(d_w) + \gamma'\, V(d_w)] \tag{3}$$

Here, $V(d_w)$ is the external volume of the structure below the groundwater table, including the collar. $A(d_w)$ is the horizontal cross-sectional area of the structure at the groundwater table. Equation (2) is Archimedes' principle. Equation (3) contains two terms. The volume term is the additional buoyancy of a fluid whose unit weight has increased by $r_u\, \gamma'$. The surface term arises because the excess pore water pressure is not zero at the groundwater table when unsaturated soil lies above it. Profile I therefore implies that the groundwater table is an undrained boundary. If this boundary drains freely, the excess pore water pressure there is zero. An alternative profile II, $\Delta u = r_u\, \gamma'(z - d_w)$, satisfies this condition. It removes the surface term, so that $U_D = r_u\, \gamma'\, V(d_w)$. The two profiles coincide when the groundwater table is at the ground surface. Profile I is used in the calculations, and profile II is used as a sensitivity case in Section 5.4. For a prismatic body with base area A and base depth z_B, Eqs. (2) and (3) reduce to $U_S = \gamma_w(z_B - d_w)A$ and $U_D = r_u\, \sigma'_{v0}(z_B)A$. These are the expressions in the design guidelines (Japan Sewage Works Association 2006; Japan Road Association 1986).

Friction is considered only above the groundwater table, where the soil is assumed not to liquefy:

$$Q_B = \int_0^{d_w} K_0 \, \gamma_t \, z \tan(2/3 \, \phi) \pi D(z) \, dz \tag{4}$$

where K_0 is the coefficient of earth pressure at rest, φ is the internal friction angle, and $D(z)$ is the outer diameter of the vertical envelope surface at depth z. The interface friction angle is taken as $2\varphi/3$. The envelope surface consists of the shaft wall, the outer surface of the soil above the cone, and the outer surface of the collar. The soil above the cone is counted once, as the weight W_S. No friction is assigned to the cone surface, so that no resistance is counted twice. The values of K_0 and of the interface friction angle were not measured. They are assumed parameters, and their influence is examined in Section 5.4.

Two results from Eqs. (1)–(3) are used in the following sections. First, setting $F_S = 1$ gives the critical excess pore water pressure ratio at the onset of uplift. For a groundwater table at the ground surface and no friction,

$$r_{u,cr} = \frac{\gamma_m - \gamma_w}{\gamma'}, \qquad \gamma_m = \frac{W_M + W_W}{V} \tag{5}$$

The apparent unit weight γ_m of the whole body, including the collar volume, is therefore the governing property. Second, the effective weight of the collar is its weight minus the pore water pressure force on its submerged volume V_c:

$$W_{W,\mathrm{eff}} = W_W - (\gamma_w + r_u \gamma') V_c \tag{6}$$

Equation (6) applies when the groundwater table is at the ground surface, as in the model tests. In the general case, the collar also replaces soil that contributed to the resistance. The change in the net resisting force caused by the collar is $\Delta R = W_W - \Delta W_S + \Delta Q_B - \Delta U_S - \Delta U_D$. Here, ΔW_S is the weight of the unsaturated soil above the cone that the collar replaces. ΔQ_B is the change in friction on the envelope surface. ΔU_S and ΔU_D are the pore water pressure forces on the submerged collar volume V_c. If the collar lies entirely above the groundwater table, $V_c = 0$ and the last two terms vanish. The nominal weight W_W is then reduced only by ΔW_S. If the collar is submerged in liquefied soil, mortar with a unit weight of 21–23 kN/m^3 displaces a fluid with a unit weight of about 19 kN/m^3. The calculated benefit is then small. In this calculation, the position of the collar relative to the groundwater table is therefore an important variable. Section 5.4 gives numerical values of each term.

2.3 Floating-Equilibrium Displacement

Assume that the soil around the manhole is liquefied to the ratio r_u and behaves as a fluid. Assume also that no shear resistance acts on the manhole. The manhole then rises until the pore water pressure force on the volume that remains below the ground surface equals its weight. For a groundwater table at the ground surface, the uplift displacement δ_f at this floating equilibrium satisfies

$$(\gamma_w + r_u\gamma')V_s(\delta_f) = W \tag{7}$$

where $V_s(\delta)$ is the external volume below the original ground surface after an uplift displacement δ, and W is the total weight. Equation (7) is solved numerically for the actual geometry. For a uniform cross-section and r_u = 1, it reduces to the expression of Tobita et al. (2012). The displacement δ_f is conditional on the assumed pressure field and on the absence of shear resistance. It is used as a reference value for the model tests. It is not a general upper bound on earthquake-induced uplift.

3. SHAKING TABLE TEST PROGRAM

3.1 Test Apparatus and Model Ground

The tests were conducted in a rigid transparent container. Its internal dimensions were 400 mm in length (the shaking direction), 300 mm in width, and 500 mm in height. The container was fixed to a uniaxial shaking table (Fig. 2). The model ground was prepared from silica sand No. 7, a uniformly graded fine sand. Table 2 lists its index properties (Japanese Geotechnical Society 2014).

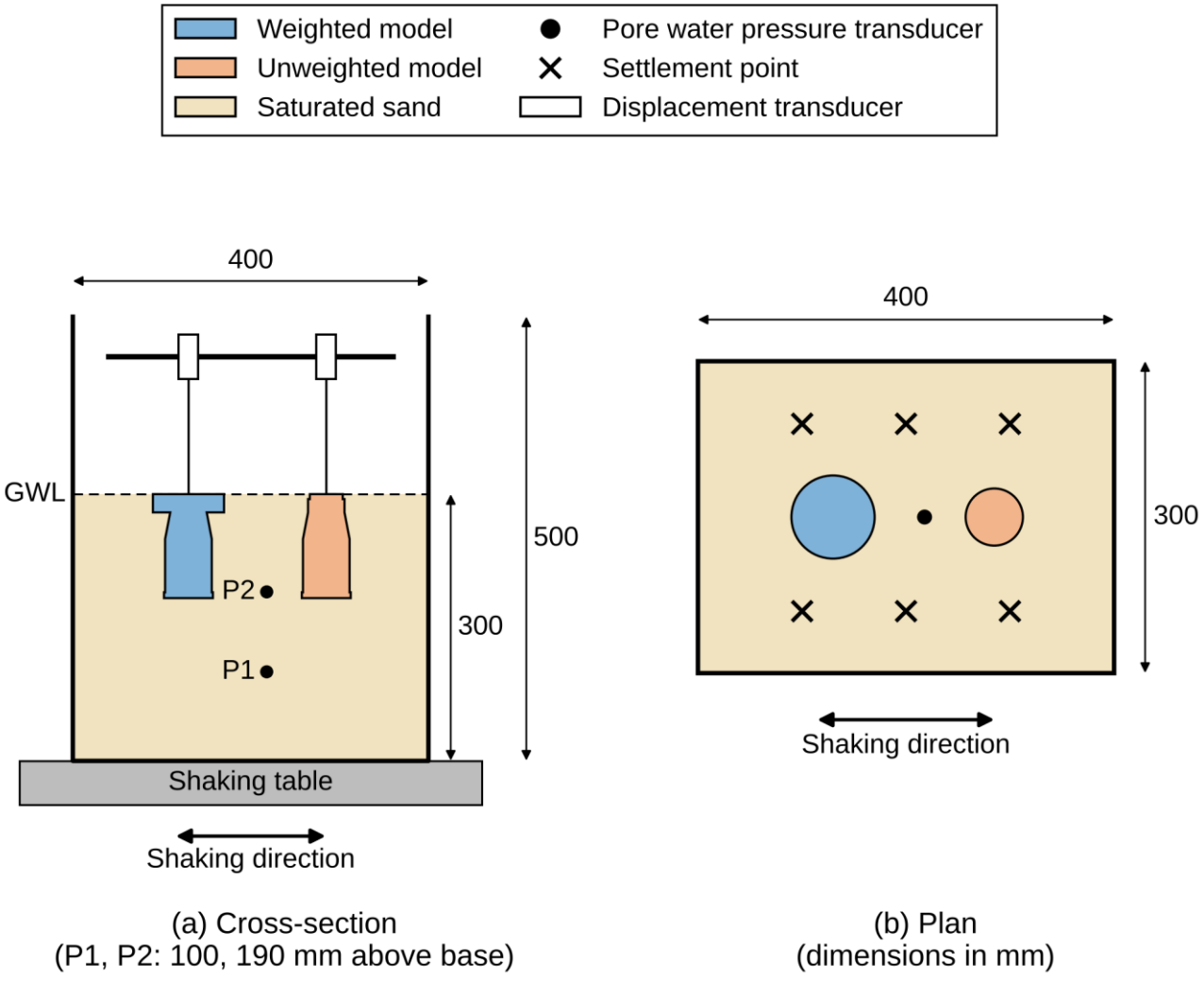

Figure 2. Arrangement of the shaking table test. The plan positions of the models are schematic.

Table 2. Index properties of silica sand No. 7 (Japanese Geotechnical Society 2014).

Property	**Value**
Soil particle density, ρ_s (g/cm^3)	2.637
Mean grain size, D_{50} (mm)	0.16
Coefficient of uniformity, U_c	1.9
Minimum dry density, ρ_{dmin} (g/cm^3)	1.272
Maximum dry density, ρ_{dmax} (g/cm^3)	1.605

The model ground was prepared by water pluviation. The container was first filled with water. Air-dried sand was then pluviated through the water from a traveling hopper. The hopper outlet was 600 mm above the container base. The hopper was moved back and forth so that the sand surface rose uniformly. Water pluviation was used to minimize entrapped air and to obtain a loose deposit without compaction. Pluviation continued until the deposit was about 300 mm thick. The water level coincided with the ground surface. The deposit is therefore described as nominally saturated. The degree of saturation was not checked independently. The groundwater table depth was zero. In the calculation of Section 2.2, this is the least favorable groundwater condition.

The mass of sand was measured in each test. The dry density was obtained by dividing this mass by the volume of the deposit minus the external volume of the two models (522.9 cm^3). The volume of the deposit is the plan area of the container (400 mm × 300 mm) multiplied by the measured thickness. The relative density was calculated as

$$D_r = \frac{\rho_{d\max}\,(\rho_d - \rho_{d\min})}{\rho_d\,(\rho_{d\max} - \rho_{d\min})} \tag{8}$$

The relative densities of the three deposits were 38.1, 39.9, and 39.3% (Table 3). All values in Table 3 follow from the masses, thicknesses, and model volumes listed there. A change of 1 mm in the measured thickness changes the relative density by about 1.5%. The differences among the three deposits are therefore within the uncertainty of the measurement. Sand in this state is loose and is used here to represent loosely placed trench backfill.

Table 3. Test cases and initial conditions of the model ground.

Quantity	Case A-50	Case A-100	Case A-150
Nominal input acceleration amplitude (m/s^2)	0.5	1.0	1.5
Frequency (Hz)	3	3	3
Prescribed double displacement amplitude of table (mm)	2.78	5.54	8.28
Thickness of deposit (mm)	297	300	295
Dry mass of sand (kg)	48.5	49.2	48.3
Volume of deposit minus volume of models (cm^3)	35,117	35,477	34,877
Dry density, ρ_d (g/cm^3)	1.381	1.387	1.385
Relative density, D_r (%)	38.1	39.9	39.3
Void ratio, e	0.909	0.901	0.904
Saturated unit weight, γ_{sat} (kN/m^3)	18.22	18.26	18.24
σ'_{v0} at transducer P1 (kPa)	1.66	1.69	1.64
σ'_{v0} at transducer P2 (kPa)	0.90	0.93	0.89

3.2 Model Manholes

The prototype is the standard No. 1 precast manhole used in Japanese sewerage works (Japan Sewage Works Association 2005). Its inner and outer diameters are 900 mm and 1,050 mm. An eccentric conical section 600 mm high reduces the outer diameter to 820 mm. The total height is 2.2 m, including the adjusting rings and the cover frame. The models are based on the external shape of the prototype at a scale of 1/20 (Fig. 3). The unweighted model represents the existing manhole. In the weighted model, a collar with an outer diameter of 80 mm and a height of 20.5 mm surrounds the neck. This collar corresponds to three weight rings and the mortar cap of the

prototype (1,600 mm by 410 mm). Exact similitude of height and mass was not achieved. Table 5 compares the prototype, the exact 1/20-scale values, and the models as tested.

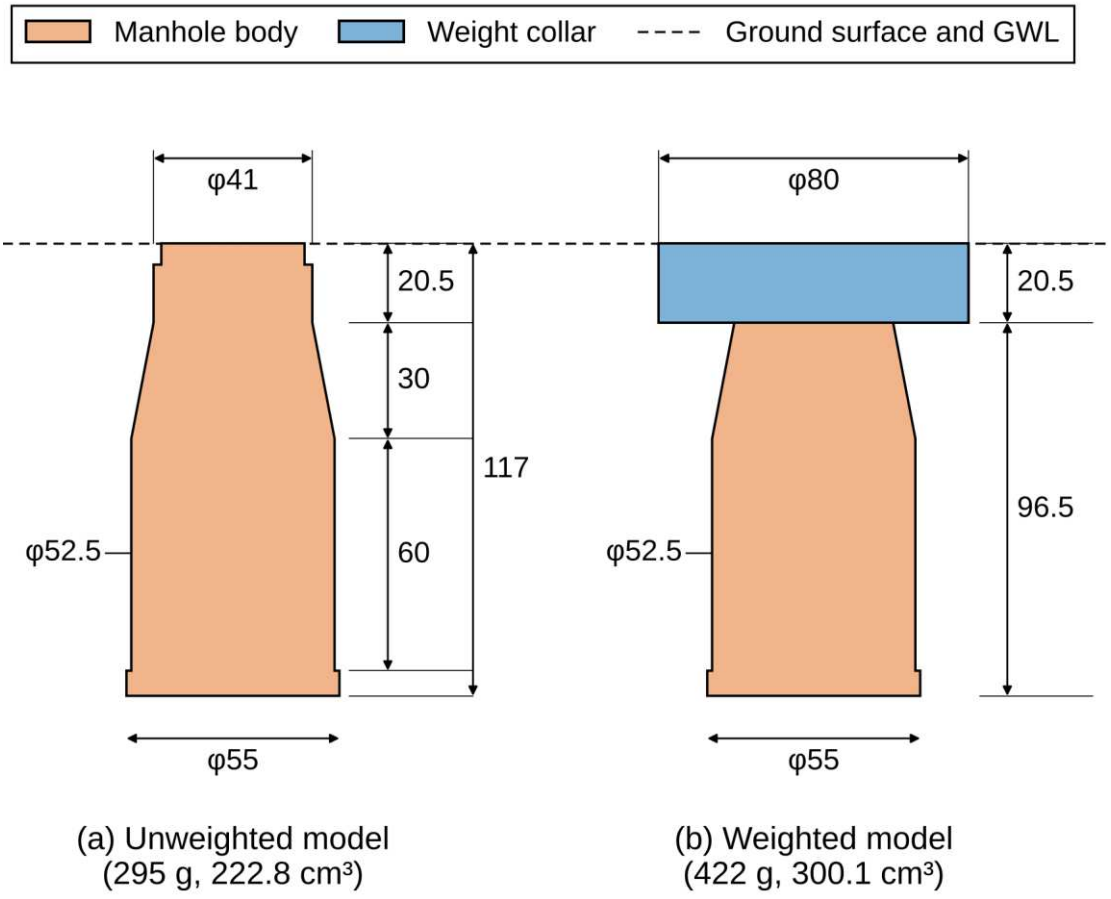

Figure 3. Model manholes at a scale of 1/20. The eccentric cone of the prototype is drawn as a symmetric cone. Dimensions are in mm.

The models were hollow and watertight. Their mass was adjusted with sand ballast placed inside. Table 4 lists the properties used in the analysis. The external volumes were calculated from the model geometry shown in Fig. 3. The collar increases the mass by 43%, from 295 g to 422 g. It also adds 77 cm^3 of displaced volume. The apparent unit weight therefore increases by only 6%, from 13.0 to 13.8 kN/m^3. Both values are much lower than the saturated unit weight of the deposit (18.2 kN/m^3). The two models differ in both mass and external geometry. The wider collar may also change the drainage and the soil–structure interaction near the ground surface. The tests therefore show the response of the complete collar configuration. They cannot separate the effect of the added weight from the effects of the changed geometry.

342 **Table 4.** Properties of the model manholes.

Property	Unweighted model	Weighted model
Total height (mm)	117	117
Outer diameter of shaft (mm)	52.5	52.5
Diameter of base slab (mm)	55	55
Outer diameter of neck or collar (mm)	41	80
Mass (g)	295	422
Weight, W (N)	2.894	4.140
External volume, V (cm^3)	222.8	300.1
Apparent unit weight, γ_m (kN/m^3)	12.99	13.79
γ_m / γ_{sat}	0.71	0.76

343

344 Table 5 compares the models with the prototype. The diameters and the collar dimensions are scaled exactly.
345 The model is 117 mm high, whereas the exact scaled height is 110 mm. Most of the difference is in the neck,
346 which is 20.5 mm high in the model and 13.5 mm at exact scale. The model collar therefore surrounds a
347 cylindrical neck, whereas the prototype collar extends over the top of the cone. The masses are not scaled exactly.
348 The unweighted model is 29% heavier than the scaled prototype, and the model collar is 27% lighter than the
349 scaled collar. As a result, the apparent unit weight of the unweighted model (13.0 kN/m^3) is higher than that of the
350 prototype (10.5 kN/m^3). The apparent unit weight of the weighted model (13.8 kN/m^3) is close to that of the
351 retrofitted prototype (13.6 kN/m^3). The model collar adds 43% to the weight, whereas the prototype collar adds
352 76%. The models therefore reproduce the external shape and the collar geometry of the prototype, but not its
353 buoyancy. These differences, together with the absence of pipes, are sources of uncertainty. Their combined effect
354 on the comparison between the two models is unresolved. The prototype is analyzed separately in Section 5.4 with
355 its own weight and geometry.

356

357 **Table 5.** Comparison of the prototype, the exact 1/20-scale values, and the models as tested.

Quantity	Prototype	Exact 1/20 scale	Model as tested
Total height	2,200 mm	110 mm	117 mm
Height of neck above the cone	270 mm	13.5 mm	20.5 mm
Outer diameter of shaft	1,050 mm	52.5 mm	52.5 mm
Diameter of base slab	1,050 mm	52.5 mm	55 mm
Outer diameter × height of collar	1,600 mm × 410 mm	80 mm × 20.5 mm	80 mm × 20.5 mm
Mass of manhole	1,825 kg	228 g	295 g
Mass of collar (three rings and mortar cap)	1,388 kg	173 g	127 g
Mass of collar / mass of manhole	0.76	0.76	0.43
External volume without collar	1.708 m^3	213.5 cm^3	222.8 cm^3
External volume with collar	2.311 m^3	288.9 cm^3	300.1 cm^3
γ_m without / with collar (kN/m^3)	10.5 / 13.6	10.5 / 13.6	13.0 / 13.8
$r_{u,cr}$ from Eq. (5) in the model deposit, without / with collar	—	0.08 / 0.45	0.38 / 0.47

358

359 The two models were placed side by side on the longitudinal centerline of the container during pluviation.
360 Their tops were level with the final ground surface. Their bases rested on pluviated sand 183 mm above the

container base. No pipes were connected to the models. The models were restrained only by the soil. The exact plan positions of the models and their clearances from the container walls were not recorded. The container is 400 mm long, so that the clear distances between the two models, and between each model and the end walls, could not exceed a few shaft diameters. Boundary and interaction effects cannot be excluded, and they were not quantified.

3.3 Instrumentation and Data Processing

The vertical displacement of each model was measured with a contact displacement transducer mounted on a fixed beam above the container. The measured displacement is absolute and positive upward. It is independent of the ground surface settlement. The readings were stored at intervals of about 1 s with a resolution of 0.001–0.005 mm. The accuracy and the calibration records of the transducers are not available.

Two pore water pressure transducers were suspended in the deposit between the models. Transducer P1 was 100 mm above the container base, and transducer P2 was 190 mm above it. The corresponding depths were about 200 mm and 110 mm. P2 was close to the level of the model bases. P1 was about 80 mm below them.

The ground surface settlement was measured after each test. The distance from a reference string to the ground surface was measured at six points on a 100 mm grid (Fig. 2). The six values were averaged.

All four channels were recorded by one data logger on a common time base for about 300 s. The record covers the shaking and most of the subsequent dissipation. The displacement records were evaluated up to t = 91, 124, and 84 s in Cases A-50, A-100, and A-150. The values at these times are referred to as the last evaluated readings. The intervals between stored readings were 0.3–0.5 s for the pore water pressure and about 1 s for the displacement. These are the intervals of the available records, and no record with a higher sampling rate exists. The 3 Hz cyclic component of the pore water pressure is therefore not resolved. It is aliased in the stored readings, and an average of aliased readings is not necessarily equal to the true cycle mean. Two of the three pore water pressure records also contain a periodic disturbance with a period of 10–12 s. The disturbance continued after shaking. Its source was not diagnosed. It may be an aliasing product or a feature of the measuring system. The records were smoothed with a centered moving average. The result is referred to as the smoothed recorded pressure. A window of 12 s was selected because it spans about one period of the disturbance. Such a window suppresses the oscillation, but it does not establish the accuracy of the resulting trend. Windows of 6 and 18 s were also applied to examine the sensitivity of the results (Section 4.3). Both the recorded and the smoothed values are shown in Section 4.

The excess pore water pressure ratio is defined as $r_u = \Delta u/\sigma'_{v0}$. The free-field initial vertical effective stress, $\sigma'_{v0} = \gamma' z$, was calculated from the density of each deposit and the nominal depth of the transducer (Table 3). The stress level in the model is very low. At the level of the model bases, σ'_{v0} is only 0.9 kPa. The resolution of the pressure records is 0.06 kPa, which is 3–7% of σ'_{v0}. The accuracy of the transducers is not documented, and their position during shaking was not measured. For illustration, a transducer that settles 10 mm in liquefied sand registers an apparent increase of about 0.18 kPa. For these reasons, the values of r_u reported below are referred to as apparent values. Pressures are reported to 0.1 kPa. Times derived from the records are reported to 1 s and were obtained by linear interpolation between stored readings. The measured quantities are the two model displacements, the two pore water pressures, the ground surface settlement after each test, the thickness of the deposit, and the mass of sand. The input motion was prescribed and was not measured. The start and end of shaking were inferred from the records (Section 3.4).

3.4 Input Motion and Time Base

The shaking table was driven with a sinusoidal horizontal motion at 3 Hz. Three nominal acceleration amplitudes were prescribed: 0.5, 1.0, and 1.5 m/s^2 (50, 100, and 150 gal). The acceleration of the table and of the container was not recorded. The amplitudes are therefore nominal values. The cases are designated A-50, A-100, and A-150. A new deposit was prepared for each case. The nominal shaking duration was 60 s. Sinusoidal input was selected so that the amplitude was the only prescribed variable among the cases.

The data logger was started a few seconds before the shaking table. Time t in this paper is the logger time. The start of shaking was identified from the first change in the pore water pressure records. It occurred at $t \approx 5$ s, with an uncertainty of about ±2 s. The end of shaking was not recorded independently. For the nominal duration of 60 s, it is at $t \approx 65 \pm 2$ s. In Case A-150, the scatter of the pore water pressure readings continued until $t \approx 87$ s. This suggests that the table was driven for about 80 s in that case. However, this duration is inferred and was not measured. The first 60 s of shaking are used for comparison among the cases. Observations in Case A-150 after $t \approx 65$ s are interpreted with this uncertainty in mind.

3.5 Similitude

Iai (1989) proposed a similitude for 1-g model tests on saturated soil–structure systems. For a geometric scale of $\lambda = 20$, the time scale is $\lambda^{0.75} \approx 9.5$. The 3 Hz input at model scale therefore corresponds to about 0.3 Hz at prototype scale. Stresses and pore water pressures scale with λ. Unit weights scale with unity. Displacements

caused by soil deformation scale with $\lambda^{1.5}$ only if the strain scaling assumed in the similitude is valid. This assumption cannot be verified at confining stresses below 2 kPa, at which sand is more dilative (Bolton 1986), and more permeable relative to its stiffness (Haigh et al. 2012), than at field stress levels. In addition, the models are not exact scaled replicas of the prototype (Table 5). The tests are therefore interpreted as exploratory observations of the two model configurations at model scale. They are not a scaled simulation of the prototype. Displacements are reported at model scale and as a fraction of the model height. They are not extrapolated to prototype scale.

4. EXPERIMENTAL RESULTS

4.1 Excess Pore Water Pressure and Liquefaction of the Model Ground

Figure 4 shows the excess pore water pressure time histories for the full recording period of 300 s. The smoothed recorded pressure and the initial vertical effective stress at each transducer are also shown.

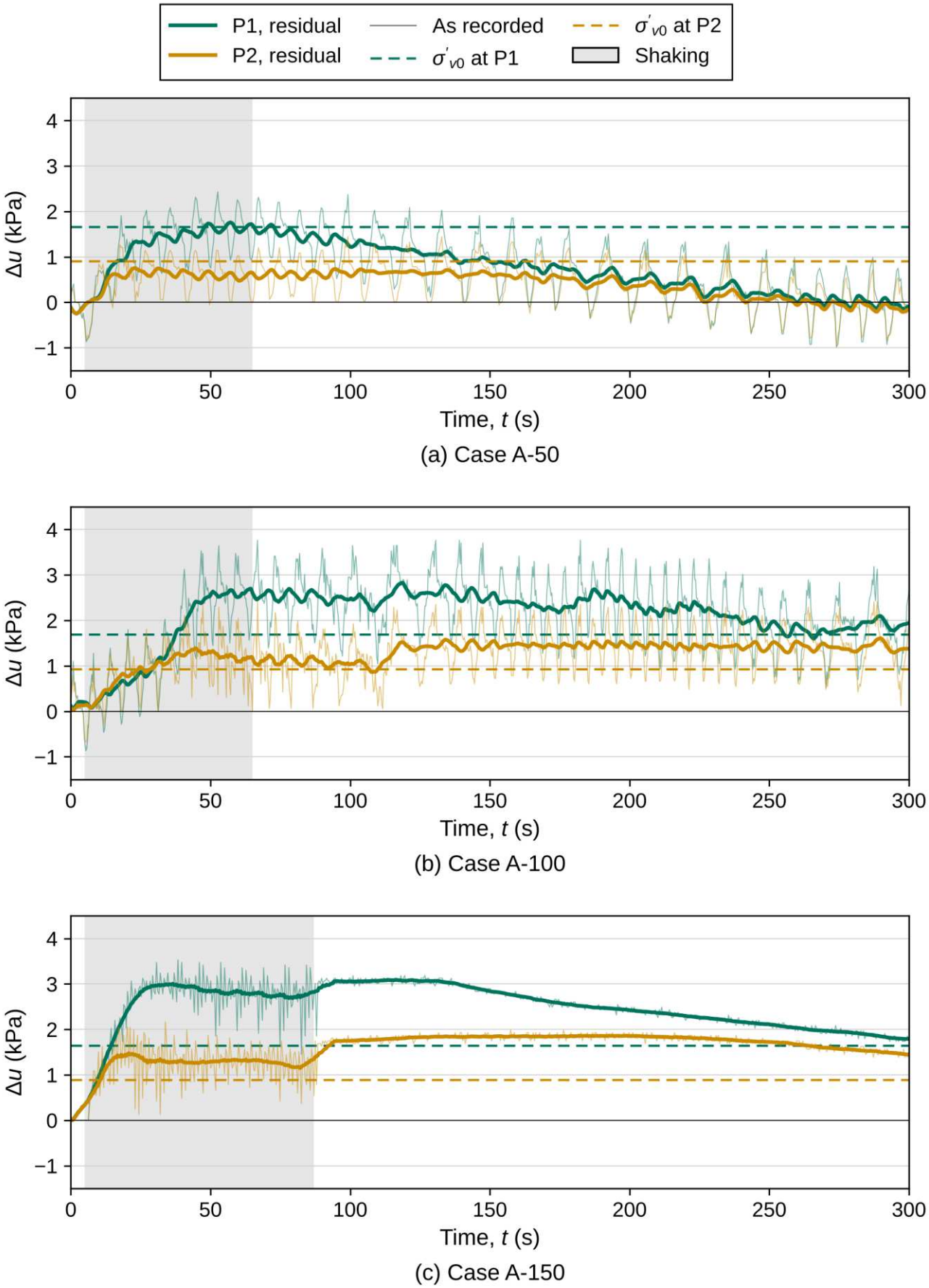

435

436 **Figure 4.** Time histories of excess pore water pressure at transducers P1 and P2.

437

In Case A-50, the smoothed excess pore water pressure at P1 began to increase at $t \approx 8$ s. It reached 1.3 kPa at about 25 s and remained at about 1.6 kPa between 40 and 65 s. The corresponding apparent r_u is about 1.0. At P2, near the level of the model bases, the smoothed value remained at about 0.6 kPa (apparent $r_u \approx 0.7$). After shaking, both values decreased gradually and returned to zero at about $t = 200$ s. At P1, the excess pore water pressure was therefore close to the estimated initial vertical effective stress. At P2, it was substantial but lower.

In Case A-100, the smoothed excess pore water pressure at P1 increased slowly to about 1.0 kPa during the first 30 s. It then increased rapidly and exceeded σ'_{v0} at $t \approx 38$ s. In Case A-150, the increase was immediate, and σ'_{v0} was exceeded at $t \approx 14$ s. In both cases, the smoothed values stabilized above the estimated initial vertical effective stress. The apparent r_u was 1.5 and 1.7 at P1 and 1.3 and 1.5 at P2 (Table 6).

A ratio greater than unity is inconsistent with the assumed reference conditions. These conditions are a transducer at its nominal depth, the estimated σ'_{v0}, and a stable zero reading. At least one of them was not satisfied. Possible causes are settlement of the transducer, a change in the local stress, a zero shift during strong shaking, and bias introduced by aliasing. For illustration, the excess of about 1 kPa at P1 corresponds to a transducer settlement of about 60 mm in liquefied sand. The transducer displacement was not measured, and the available data cannot separate these causes. The ratios above unity are therefore treated as evidence of uncertainty in the pressure magnitude, and they are not corrected. The records support a more limited statement. In Cases A-100 and A-150, the excess pore water pressure at both instrumented depths was of the order of the estimated initial vertical effective stress or greater. In Case A-50, this was the case only at P1. No pressure was measured at shallower depths, around the shafts, or beneath the collar. The pressure distribution over the embedded height of the models is therefore unknown.

Two further observations are consistent with extensive liquefaction of the deposit. First, the excess pore water pressure in Cases A-100 and A-150 was sustained for more than 200 s after shaking, and the ground surface settled by 13–14 mm. An illustrative order-of-magnitude calculation relates these two values. Assume that the pore water is expelled upward over the full plan area under a hydraulic gradient of $\gamma'/\gamma_w \approx 0.86$. The Darcy velocity then equals the settlement rate (Scott 1986). A settlement of 13.8 mm in 200–300 s gives a coefficient of permeability of $5–8 \times 10^{-5}$ m/s. This value is not a measured soil property. It shows only that the duration and the settlement are compatible with a fine sand. Second, the volumetric strain of the deposit after each test was 3.8, 4.5, and 4.7%. These values are of the magnitude given by the chart of Ishihara and Yoshimine (1992) for liquefied loose sand. The smaller value in Case A-50 is consistent with the lower excess pore water pressure in the upper part of that deposit.

In Case A-150, the smoothed excess pore water pressure at P2 increased from 1.3 to 1.8 kPa at $t \approx 87$ s, when the scatter of the readings ceased. This time is the inferred end of shaking (Section 3.4). One possible explanation is cyclic dilation. Each cycle of shear strain in sand at very low confining stress may cause a transient decrease in pore water pressure. The average during shaking would then be lower than the value at rest. Other explanations are redistribution of pore water pressure after shaking, a change in the aliasing bias when the cyclic component stops, and movement of the transducer. The records do not resolve the cyclic response, and the timing is inferred. The cause therefore cannot be identified. The observation is noted because it bears on the back-analysis in Section 5.2.

Table 6. Summary of measured response.

Quantity	A-50	A-100	A-150
Smoothed Δu at P1, mean for t = 40–65 s (kPa)	1.6	2.5	2.8
Smoothed Δu at P2, mean for t = 40–65 s (kPa)	0.6	1.2	1.3
Apparent r_u at P1 / P2	1.0 / 0.7	1.5 / 1.3	1.7 / 1.5
Maximum uplift displacement of unweighted model (mm)	9.57	10.10	13.98
Maximum uplift displacement / manhole height (%)	8.2	8.6	11.9
Mean uplift rate, 10–90% of maximum (mm/s)	0.27	0.35	0.40
Uplift displacement of unweighted model at last evaluated reading (mm)	9.57	9.29	12.92
Maximum settlement of weighted model (mm)	0.98	0.40	0.69
Displacement of weighted model at last evaluated reading (mm)	−0.98	−0.24	−0.67
Mean ground surface settlement (mm)	11.3	13.5	13.8
Volumetric strain of deposit (%)	3.8	4.5	4.7
Estimated protrusion above mean settled ground surface, unweighted model (mm)	20.9	22.8	26.7
Estimated protrusion above mean settled ground surface, weighted model (mm)	10.3	13.3	13.1

4.2 Vertical Displacement of the Model Manholes

Figure 5 compares the vertical displacement time histories of the two models.

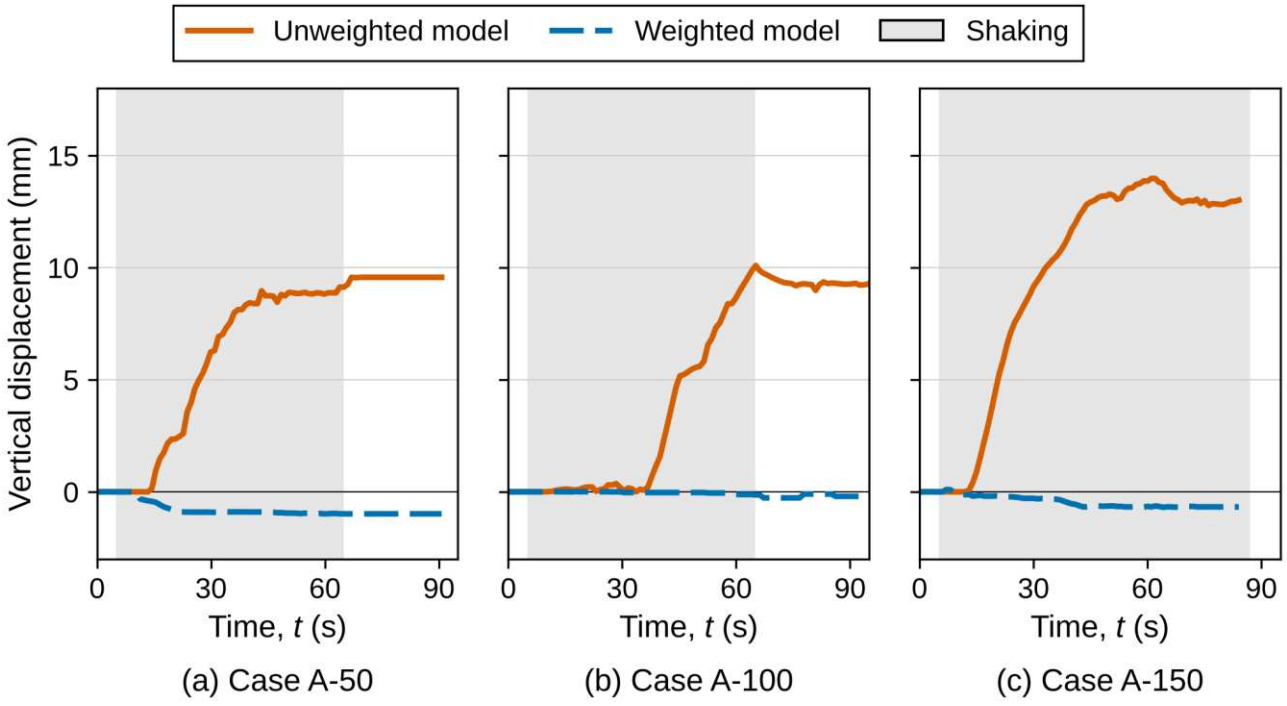

Figure 5. Time histories of vertical displacement of the model manholes (positive upward).

The unweighted model was uplifted in every test. In Case A-50, uplift began at $t \approx 15$ s, and the uplift rate decreased with time. Between $t \approx 45$ and 62 s, the displacement was nearly constant at 8.8–8.9 mm. It then increased to 9.57 mm at $t \approx 67$ s and remained at this value. This last increase occurred near the inferred end of shaking (65 ± 2 s). Whether it occurred before or after the end of shaking cannot be determined. In Case A-100, the model moved by only 0.1–0.3 mm during the first 30 s. It then rose steadily from $t \approx 37$ s and reached 10.10 mm at $t \approx 65$ s. No plateau was reached. The uplift rate was still about 0.3 mm/s when the displacement reached its maximum. The model subsequently settled by 0.8 mm. In Case A-150, uplift began at $t \approx 14$ s. The initial uplift rate was the highest of the three cases. The rate decreased to less than 0.1 mm/s after $t \approx 45$ s. The displacement reached a maximum of 13.98 mm at $t \approx 61$ s. The model then settled by about 1 mm and remained at 12.9 mm from $t \approx 72$ s to the last evaluated reading.

The maximum uplift displacement corresponds to 8.2, 8.6, and 11.9% of the manhole height. It increased with the nominal input acceleration amplitude. The mean uplift rate also increased (0.27, 0.35, and 0.40 mm/s).

Three features of these time histories are similar to those of previous 1-g and centrifuge model tests (Koseki et al. 1997a; Tobita et al. 2011; Chian et al. 2014). Most of the uplift accumulated during shaking. The uplift rate increased with the shaking intensity. Uplift was followed by a small settlement. Whether uplift stopped exactly at the end of shaking cannot be resolved, because the end of shaking is known only to within about ±2 s. A fourth feature concerns Cases A-50 and A-150. In these cases, the uplift rate decreased markedly while shaking

continued, and the displacement approached a nearly constant value. In Case A-100, no such plateau was observed. This behavior is examined in Section 5.

The weighted model showed no measurable uplift in any test. In Case A-50, it settled by 0.9 mm between t = 10 and 20 s as the excess pore water pressure increased. It then remained nearly stationary. In Case A-100, it did not move until the last seconds of shaking. It settled by 0.3 mm at that stage and by 0.4 mm at most. In Case A-150, it settled gradually to 0.7 mm. These displacements are one order of magnitude smaller than the uplift of the unweighted model and opposite in direction. As noted in Section 3.2, this difference is the response of the complete collar configuration. It cannot be attributed to the added weight alone.

Figure 6 shows the two models after Case A-150. The neck and part of the conical section of the unweighted model are exposed above the ground surface. The top of the weighted model appears to be close to the local soil surface and is partly covered by a thin layer of sand. This impression refers to the local surface next to the model. The sand layer is interpreted as ejected or displaced sand, but it was not measured. The photograph does not show that the protrusion was negligible. The six-point mean settlement of the ground surface in this case was 13.8 mm. The estimated protrusion of the weighted model above the mean settled surface is about 13 mm (Section 4.4).

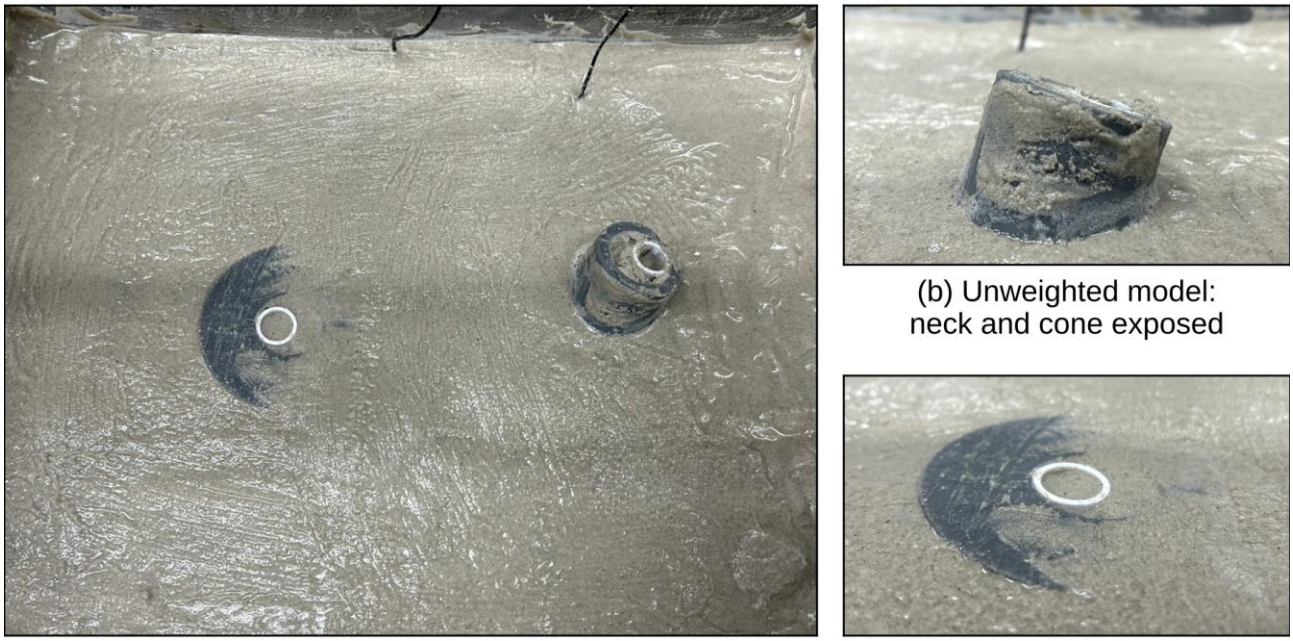

Figure 6. Model manholes after Case A-150.

4.3 Relationship Between Uplift and Excess Pore Water Pressure

Figure 7 shows the uplift displacement of the unweighted model plotted against the apparent r_u at P1. Table 7 summarizes the times of liquefaction and uplift.

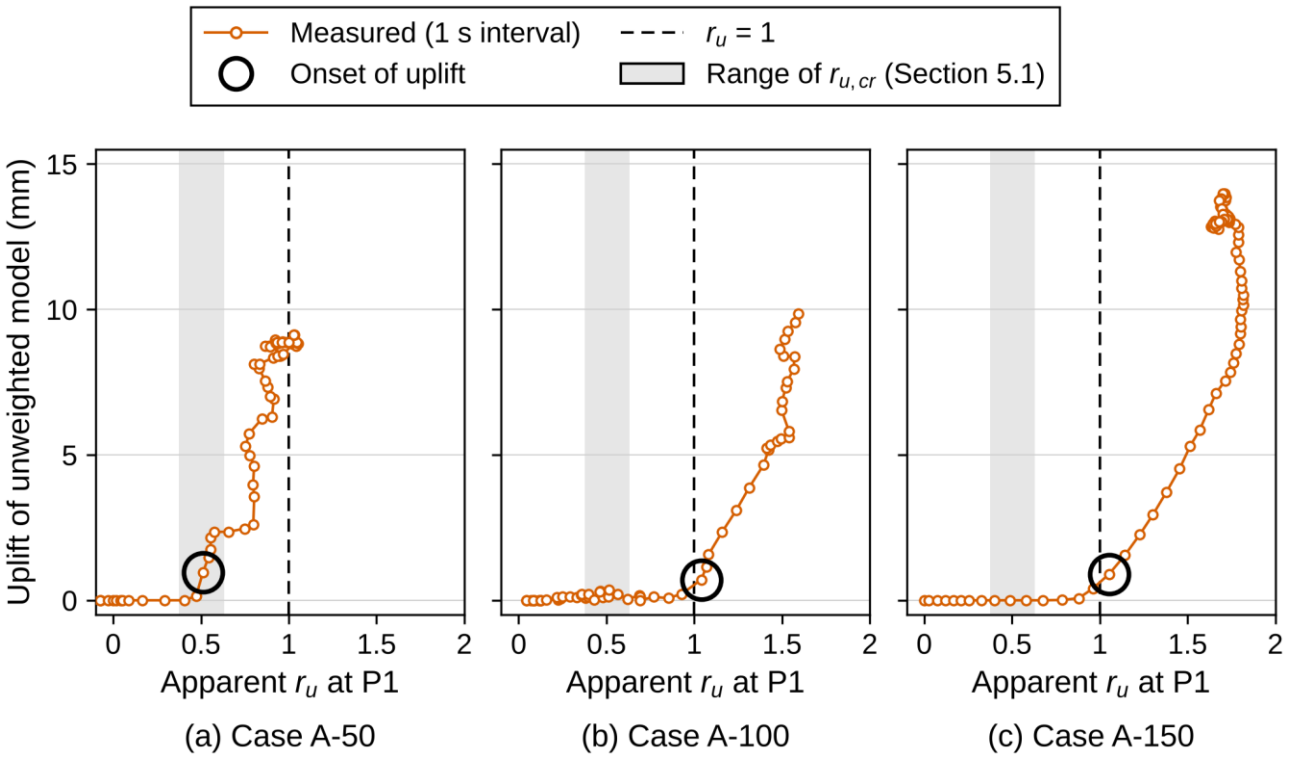

Figure 7. Relationship between the uplift displacement of the unweighted model and the apparent excess pore water pressure ratio at P1 during shaking.

Table 7. Times of excess pore water pressure buildup and uplift (logger time; shaking starts at t ≈ 5 ± 2 s; times are rounded to 1 s).

Quantity	A-50	A-100	A-150
Onset of uplift, δ > 0.5 mm (s)	15	38	15
Onset of uplift for thresholds of 0.3 / 1.0 mm (s)	15 / 16	26 / 39	14 / 16
Smoothed Δu at P1 at onset of uplift (kPa)	0.8	1.8	1.7
Apparent r_u at P1 / P2 at onset of uplift	0.5 / 0.7	1.0 / 1.4	1.1 / 1.5
Time at which smoothed Δu at P1 reached σ'_{v0}, window of 6 / 12 / 18 s (s)	29 / 48 / 52	39 / 38 / 39	14 / 14 / 15
Time at which smoothed Δu at P1 reached $0.8\sigma'_{v0}$, window of 6 / 12 / 18 s (s)	20 / 23 / 28	35 / 35 / 34	12 / 12 / 13
Time of maximum uplift displacement (s)	67	65	61

Table 7 lists the time at which the smoothed excess pore water pressure at P1 reached the estimated σ'_{v0} for three window lengths. In Cases A-100 and A-150, this time is insensitive to the window (38–39 s and 14–15 s). In Case A-50, it varies from 29 to 52 s, because the pressure approached σ'_{v0} gradually. The onset of uplift, defined by a displacement of 0.5 mm, was at $t \approx 38$ s in Case A-100 and at $t \approx 15$ s in Case A-150. In these two cases,

uplift therefore began at about the time when the pressure at P1 reached the estimated σ'_{v0}. The two times agree within 1–2 s, which is the resolution of the displacement record and of the time base. A closer coincidence cannot be claimed. In Case A-100, a displacement of 0.3 mm was reached at $t \approx 26$ s. However, the displacement remained below 0.5 mm until $t \approx 38$ s, although the pressure at P1 had been about half of σ'_{v0} for about 20 s. Case A-50 differs from the other two cases. Uplift began at $t \approx 15$ s, when the apparent r_u was only 0.4–0.5 at P1 and 0.5–0.7 at P2. Uplift then continued while the pressure at P1 increased toward σ'_{v0}. A pressure equal to σ'_{v0} at the instrumented depths was therefore not a necessary condition for the onset of uplift. After the onset, the displacement accumulated while the apparent r_u changed little. The curves in Fig. 7 therefore become steep.

The time required for the pressure buildup did not decrease monotonically with the nominal input acceleration amplitude. The pressure at P1 reached σ'_{v0} after about 10 s of shaking in Case A-150 and after about 33 s in Case A-100. In Case A-50, the excess pore water pressure at P2 reached its plateau after about 10 s. A new deposit was used in each case, and the differences in relative density are within the measurement uncertainty. The input acceleration was not recorded. The cause of the delayed buildup in Case A-100 cannot be determined from the available measurements. Both models were in the same deposit and were subjected to the same table motion in each case. The comparison between them is therefore less affected by this variation than a comparison between separate tests.

4.4 Ground Surface Settlement and Estimated Protrusion

The mean ground surface settlement was 11.3, 13.5, and 13.8 mm. It was measured at six points after each test. The displacement transducers measure absolute displacement. The protrusion of a model above the surrounding ground was not measured directly. It is estimated as the sum of the last evaluated displacement of the model and the mean ground surface settlement (Fig. 8). The two measurements are not synchronous, because the settlement was measured after the end of the record. The estimate also refers to the mean surface and not to the local surface next to the model. The true local step therefore cannot be determined precisely. The estimated protrusion was 21–27 mm for the unweighted model and 10–13 mm for the weighted model. For the weighted model, the entire estimated protrusion results from settlement of the loose deposit around a model that remained nearly stationary.

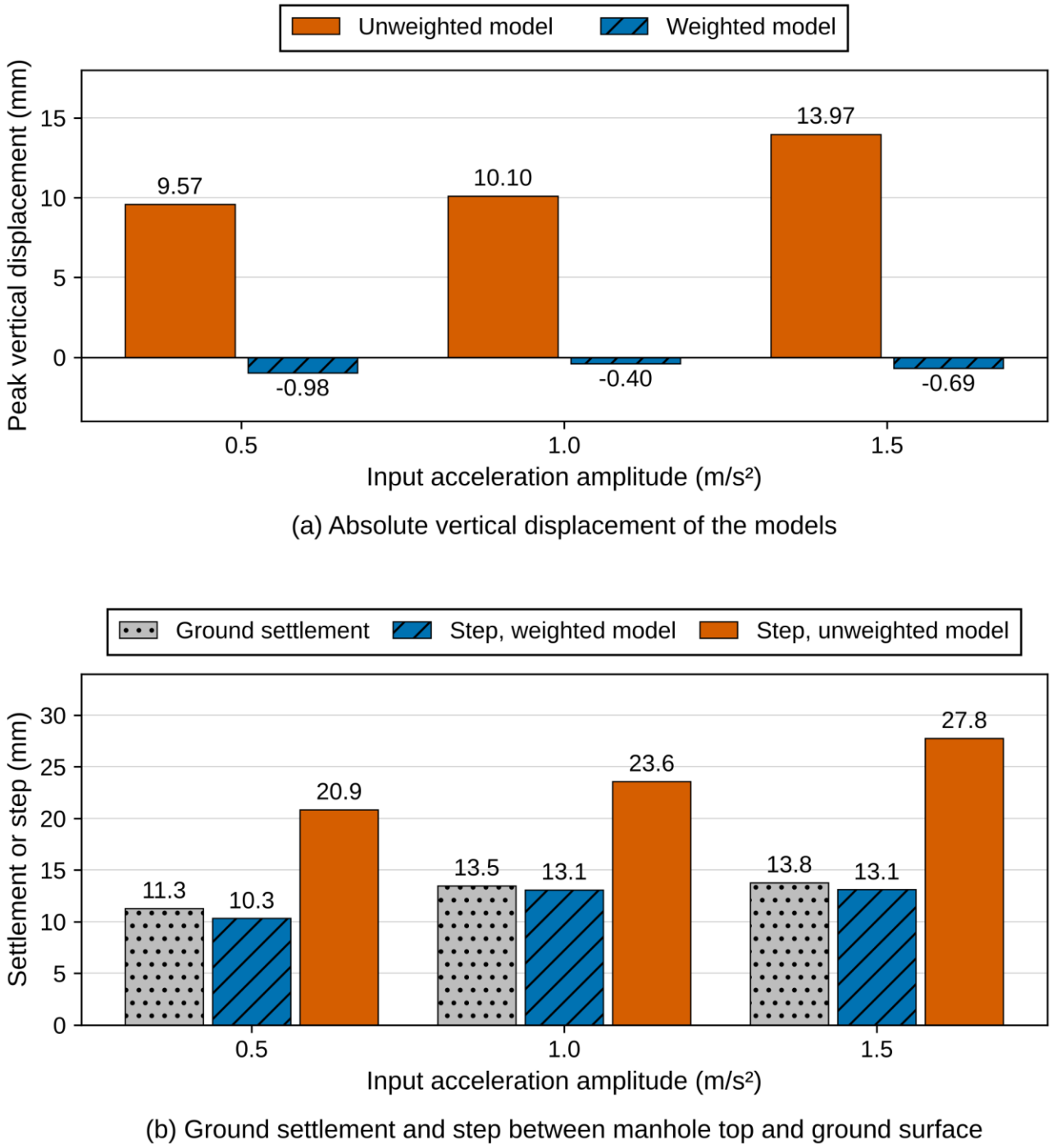

566

567 **Figure 8.** Summary of model displacements, ground surface settlement, and estimated protrusion.

568

569 This distinction is important for post-earthquake functionality. In the weighted model, the uplift component
570 of the protrusion was absent, and the estimated protrusion was about half of that of the unweighted model. The
571 collar does not reduce the reconsolidation settlement of the surrounding soil, and it is not intended to do so. The
572 volumetric strains of 4–5% measured here correspond to a very loose deposit at model stress levels. They are
573 probably larger than the strains of compacted backfill beneath a pavement, and the model-scale protrusion cannot
574 be converted to a prototype step height (Section 3.5). Nevertheless, the result indicates that a weighted manhole in

loose ground may protrude above a settled road surface even though it has not been uplifted. For road access after an earthquake, the relevant quantity is the step between the manhole and the adjacent road surface, and not the absolute uplift alone. No pipes were connected to the models. Suppression of absolute uplift may reduce one source of relative displacement at pipe joints. However, a stationary manhole can still move relative to settling ground and pipes. The performance of pipe connections, and hence the continuity of wastewater service, is outside the scope of this study.

5. ANALYTICAL INTERPRETATION

The analysis consists of four steps. First, the limit equilibrium formulation of Section 2.2 is applied to the two models. Second, the displacement of the unweighted model is back-analyzed to obtain an equivalent excess pore water pressure ratio. Third, the time history of uplift is described by a first-order model. Fourth, the formulation is applied to one prototype configuration as an illustration. The second and third steps use the displacement records that the analysis seeks to explain. They are therefore an interpretation of the tests and not an independent verification. All quantities were calculated numerically from the axisymmetric profiles of the models (Fig. 3) and of the prototype. The eccentricity of the cone does not affect the volumes or the vertical force resultants.

5.1 Limit Equilibrium of the Model Manholes

For a groundwater table at the ground surface and no friction, Eqs. (1)–(3) reduce to $F_S = W / [(\gamma_w + r_u \gamma')V]$. Two limiting scenarios are considered for the weighted model. In case A, the excess pore water pressure ratio is uniform over the full depth. The collar is then subjected to both hydrostatic and excess pore water pressure. In case B, no excess pore water pressure acts on the underside of the collar. The collar is then subjected to hydrostatic pressure only. The underside is only 20.5 mm below a free-draining surface, where the initial vertical effective stress is 0.17 kPa. The pressure at this location was not measured. Cases A and B are therefore limiting analytical scenarios and not identified pressure conditions. Figure 9 shows the factor of safety as a function of r_u.

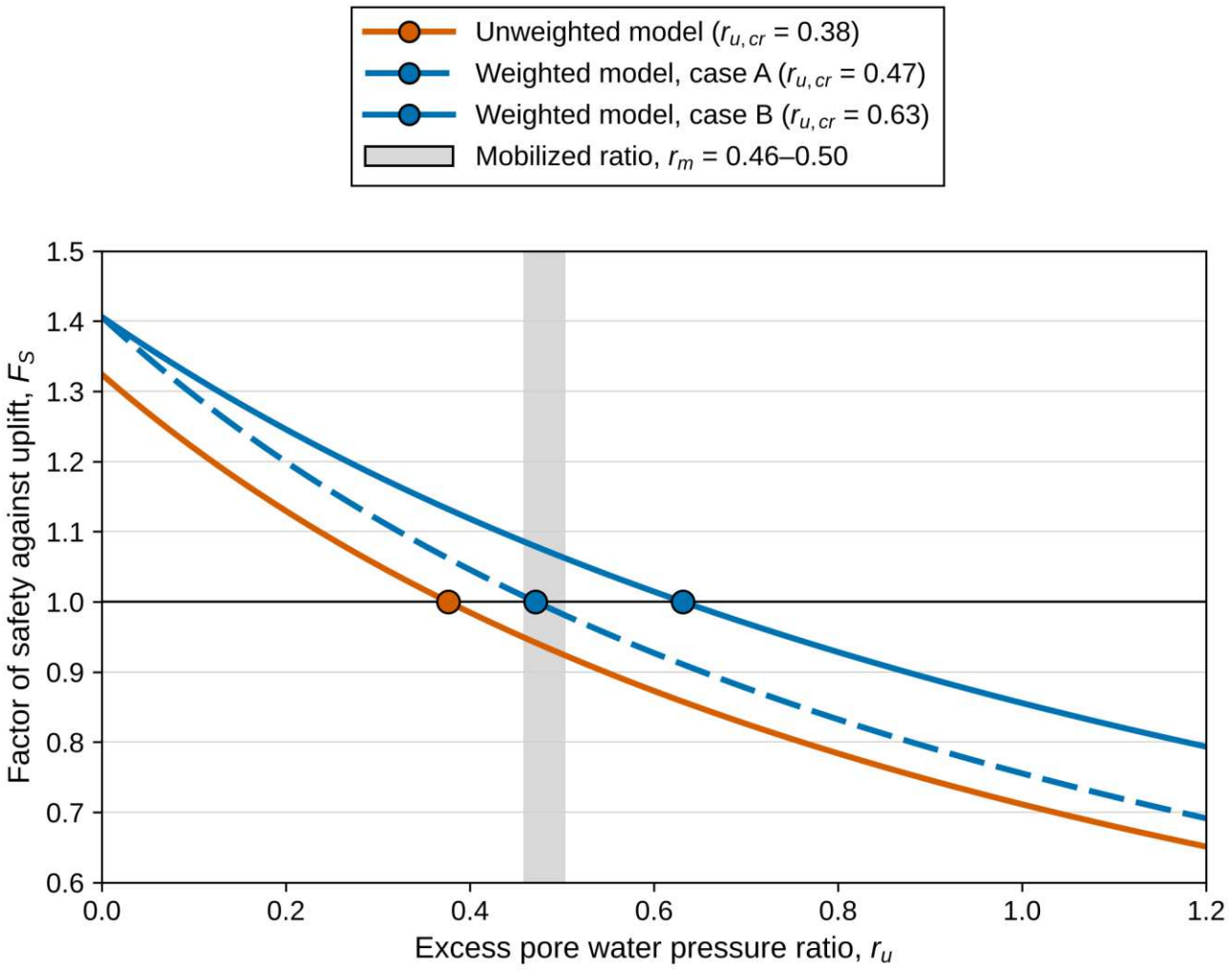

Figure 9. Factor of safety against uplift of the model manholes as a function of the excess pore water pressure ratio. The shaded band is the range of the back-calculated equivalent ratio (Section 5.2). Circles indicate the critical ratios at $F_S = 1$.

Before shaking ($r_u = 0$), both models are stable. The factors of safety are 1.32 and 1.41. The critical ratio for the unweighted model is 0.38. For the weighted model, it is 0.47 in case A and 0.63 in case B. At full liquefaction ($r_u = 1$), the factor of safety is 0.71 for the unweighted model. It is 0.76 (case A) or 0.86 (case B) for the weighted model. The floating-equilibrium displacement from Eq. (7) at $r_u = 1$ is 44 mm for the unweighted model. For the weighted model, it is 15 mm in case A and 12 mm in case B. These values were obtained from the actual volume function $V_s(\delta)$. In the weighted model, the collar emerges first, so that a small displacement removes a large volume. The pressure integration neglects the effective weight of the saturated soil above the cone. If this weight is added to the resistance, the critical ratios become 0.45, 0.49, and 0.65. The interpretation below does not depend on this choice.

The assumption of full liquefaction therefore predicts that both models are uplifted. Equation (6) shows why the calculated benefit of the collar is small in this condition. The collar weighs 1.25 N, but it adds 77 cm^3 of displaced volume. The hydrostatic force on this volume alone is 0.76 N. At r_u = 1, the effective weight of the collar is +0.49 N in case B and −0.17 N in case A. In case A, the collar is slightly lighter than the liquefied soil that it displaces. With the groundwater table at the ground surface, the test condition was the least favorable condition for the retrofit in this calculation.

The test results differ from this prediction in two respects. First, the unweighted model was uplifted by only 9.6–14.0 mm, which is 22–32% of the floating-equilibrium displacement. In Cases A-50 and A-150, the uplift rate had decreased markedly before the end of shaking. Second, the weighted model was not uplifted. Within the force balance of Section 2.2, both differences can be represented by a net uplift force smaller than the full-liquefaction value. Unmodeled resistance would have the same effect. The two cannot be distinguished with the available data.

5.2 Equivalent Excess Pore Water Pressure Ratio

An equivalent uplift force can be back-calculated from the displacement of the unweighted model. The reference elevations are as follows. The displacement δ is measured relative to a fixed beam. The original ground surface coincides with the initial top of the model and with the water level. The water expelled from the settling deposit remains above the soil. The water level is therefore assumed to stay at its original elevation. The soil surface settled by 11–14 mm, but its settlement history during shaking is unknown. When the model has been uplifted by δ, the volume below the original surface decreases to $V_s(\delta)$. Assume that the model is then in equilibrium under its weight and a pore water pressure field described by a single ratio r_m, with no other resistance. This ratio is

$$r_m = \frac{1}{\gamma'}\left[\frac{W}{V_s(\delta)} - \gamma_w\right] \tag{9}$$

The ratio r_m is an equivalent parameter. It is conditional on the force balance of Section 2.2 and on the equilibrium assumption. It includes the effects of unmodeled resistance, geometric approximation, drainage, and uncertainty in the reference elevations. It is not a measured excess pore water pressure ratio at the surface of the model. Equation (9) with the maximum uplift displacement of each case gives r_m = 0.46, 0.46, and 0.50 for Cases A-50, A-100, and A-150 (Table 8). The equilibrium assumption is supported to a different degree in each case. In Case A-50, the displacement was nearly constant between $t \approx 45$ and 62 s, and the plateau value of 8.9 mm gives

r_m = 0.45. In Case A-150, the uplift rate had decreased to less than 0.1 mm/s. In Case A-100, no plateau was reached. The value for this case is therefore an apparent, displacement-based value and not an equilibrium value. The asymptotic displacement from the first-order fit of Section 5.3 gives 0.46, 0.50, and 0.51. The settlement of the soil surface defines an alternative end state. Assume that the excess pore water pressure acts only on the volume below the finally settled soil surface, whereas the hydrostatic pressure acts up to the original water level. Then r_m becomes 0.49, 0.51, and 0.55. The settlement history is unknown, so that these values and those of Eq. (9) bracket the result. Over all interpretations, r_m is about 0.45–0.55. In contrast, the apparent ratios from the transducers ranged from 0.7 to more than 1.

Several effects may contribute to a value of r_m below unity. None of them was identified experimentally, and the available data do not allow them to be separated.

- *Cyclic dilation.* At low confining stress, loose sand can dilate in each half cycle of shear (Bolton 1986). The pore water pressure adjacent to a structure that moves relative to the soil may then decrease transiently. The average during shaking may be lower than the value at rest. The increase at P2 at the inferred end of shaking in Case A-150 (1.3 to 1.8 kPa) is compatible with this effect. However, other explanations are possible (Section 4.1).
- *Partial drainage.* The models were embedded in the upper 117 mm of a deposit with a free-draining surface. In Case A-50, the apparent ratio near the level of the model bases was about 0.7, whereas the ratio 90 mm deeper was about 1.0.
- *Shear resistance.* Equation (9) neglects the friction on the shaft and the resistance to the flow of soil beneath the base. Any such resistance appears as a reduction in r_m.
- *Reference elevation.* The soil surface settled by 11–14 mm relative to the container. The part of this settlement that occurred during uplift is unknown. It changes the embedded volume, as the alternative values in Table 8 show.

The equivalent ratio can be transferred to the weighted model only by assumption. The assumption is that the same equivalent ratio applies to both models, although the collar changes the local geometry and possibly the pressure field. Under this assumption, the factor of safety of the weighted model follows from Fig. 9. For r_m = 0.45–0.55, it is 0.95–1.01 in case A and 1.04–1.09 in case B. With the case-by-case values of Table 8, it is 0.97–1.05 in case A and 1.06–1.09 in case B. These values are close to unity, and some are slightly below it. A difference of a few percent is within the uncertainty of the calculation. The calculation is therefore a consistency check for the late stage of shaking. It does not describe the stability history, and it is not an independent

validation. It shows that one equivalent pressure condition is compatible with both observations. These are the uplift of the unweighted model, whose critical ratio is 0.38, and the absence of uplift of the weighted model, whose critical ratio is 0.47–0.63. Other combinations of pressure and resistance may be equally compatible.

Table 8. Results of the back-analysis and of the first-order fit (± one standard error of the fit).

Quantity	A-50	A-100	A-150
Maximum uplift displacement of unweighted model, δ_{max} (mm)	9.57	10.10	13.98
δ_{max} / floating-equilibrium displacement from Eq. (7)	0.22	0.23	0.32
Equivalent ratio, r_m, from Eq. (9) with δ_{max}	0.46	0.46	0.50
r_m with fitted asymptote δ_∞	0.46	0.50	0.51
r_m with δ_{max} and settled soil surface	0.49	0.51	0.55
F_S of weighted model at r_m, case A / case B	1.01 / 1.09	1.00 / 1.08	0.98 / 1.06
F_S of weighted model with settled soil surface, case A / case B	1.05 / 1.08	1.05 / 1.08	1.03 / 1.06
Fitted start of uplift, t_0 (s)	15	36	14
Fitting interval (s) / number of readings	14–62 / 47	36–65 / 27	13–61 / 48
Asymptotic uplift displacement, δ_∞ (mm)	9.7 ± 0.2	13.8 ± 1.4	14.9 ± 0.1
Time constant, τ (s)	14.7 ± 1.2	23.8 ± 4.3	16.7 ± 0.5
Coefficient of determination, R^2	0.97	0.98	1.00
Range of δ_∞ (mm) / τ (s) for shifted fitting intervals	9.6–10.0 / 13.9–15.8	12.0–14.6 / 19.1–26.6	14.8–14.9 / 16.4–16.8
Buoyant stiffness, k (N/m)	18.1	18.6	18.7
Resistance coefficient, $c = k\tau$ (N·s/m)	270	440	310

This interpretation has clear limitations. The difference between the critical ratio of the weighted model and the equivalent ratio is small and lies within the uncertainty of both. The calculated stability of the weighted model depends on an equivalent uplift force that is lower than that of full liquefaction. The result does not show that a collar submerged in fully liquefied soil is adequate. It shows that, in these tests, the equivalent uplift force on the unweighted model was about half of the full-liquefaction value. The absence of uplift of the weighted model is compatible with this value.

5.3 Time History of Uplift

The displacement time histories in Fig. 5 show a decreasing uplift rate in Cases A-50 and A-150. A first-order model is used to describe this slowly varying displacement envelope. The cyclic response is not resolved and is not modeled. Assume that the liquefied soil exerts a resistance c dδ/dt on the rising manhole. The inertia of the envelope motion is neglected because uplift takes tens of seconds. Vertical equilibrium then gives

$$c\,\frac{d\delta}{dt} = (\gamma_w + r_m\gamma')V_s(\delta) - W \;\approx\; F_0 - k\,\delta \tag{10}$$

where F_0 is the net uplift force at the onset of uplift and r_m is the equivalent ratio of Section 5.2. The buoyant stiffness is $k = (\gamma_w + r_m \gamma')A_n$. It arises because each increment of uplift removes a volume A_n δ of the neck from the pore water pressure field. The cross-sectional area of the neck is A_n = 1,320 mm^2. For uplift that starts at time t_0, the solution is

$$\delta(t) = \delta_\infty \left[1 - \exp\left(-\frac{t - t_0}{\tau}\right)\right], \qquad \delta_\infty = \frac{F_0}{k}, \quad \tau = \frac{c}{k} \tag{11}$$

Equation (11) was fitted to each record by nonlinear least squares. The free parameters were δ_∞, τ, and t_0. The fitting intervals were t = 14–62 s, 36–65 s, and 13–61 s. In Case A-50, the interval ends before the final increase near the end of shaking. Table 8 lists the estimates and their standard errors. The sensitivity was examined by shifting the ends of the fitting interval by a few seconds (Fig. 10 and Table 8).

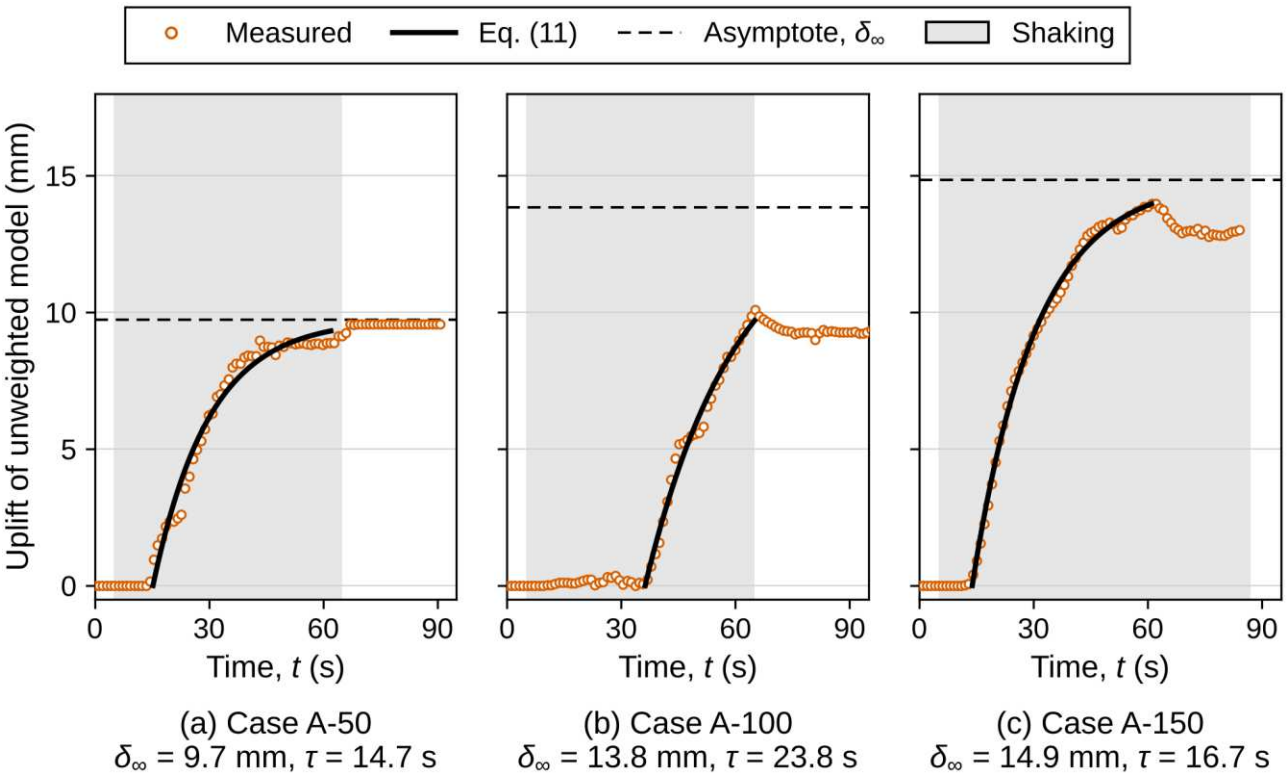

Figure 10. First-order uplift model, Eq. (11), fitted to the measured uplift displacement of the unweighted model.

The model describes all three records closely (R^2 = 0.97–1.00). A close fit does not identify the mechanism. Other functions with a decreasing rate would describe the records equally well. Equation (11) is therefore used as a phenomenological description. The time constants are 14.7 ± 1.2, 23.8 ± 4.3, and 16.7 ± 0.5 s. In Cases A-50

and A-150, the fitting interval covers about three time constants, and the asymptotic displacements (9.7 and 14.9 mm) are well constrained. The measured maximum displacements are 94–98% of these values. In Case A-100, the pressure buildup was delayed, and only about 29 s of uplift was recorded. The asymptote was not approached. The fitted value of 13.8 ± 1.4 mm is an extrapolation, and it varies between 12.0 and 14.6 mm with the fitting interval. The measured maximum is 73% of this value. The two analyses of Case A-100 are therefore separate approximations with different assumptions. Equation (9) with δ_{max} assumes that the model was in equilibrium at its maximum displacement and gives $r_m = 0.46$. The first-order fit assumes that uplift would have continued to δ_∞ under an unchanged pressure field and gives $r_m = 0.50$. The two values cannot represent the same equilibrium state. For Case A-100, the first is a lower estimate, and the second is an extrapolated estimate. The similar maximum displacements in Cases A-50 and A-100 (9.6 and 10.1 mm) may therefore reflect the shorter time available for uplift in Case A-100.

With $k \approx 18$–19 N/m, the fitted time constants correspond to resistance coefficients of about 270–440 N·s/m. These coefficients are model-scale fitting parameters and not material properties. A dimensional comparison with apparent viscosities reported for liquefied sand (Hwang et al. 2006) is possible, but it has no significance for a confined, non-spherical model in a non-Newtonian soil and is not pursued. Resistance to the flow of soil toward the space beneath the base has been proposed as a controlling process (Koseki et al. 1997a; Chian et al. 2014; Chou et al. 2011). The present data are compatible with this process but do not demonstrate it.

Two observations follow for the tested models. First, the displacement depended on the time available for uplift relative to the time constant. This agrees with the influence of the shaking duration in centrifuge model tests (Tobita et al. 2011). Second, the uplift rate decreased as the neck emerged. The model represents this effect by the buoyant stiffness k. A factor of safety alone represents neither effect. Neither effect can be transferred quantitatively to a prototype on the basis of these tests.

5.4 Illustrative Calculation at Prototype Scale

The formulation of Section 2.2 was applied to the prototype No. 1 manhole as an illustration. Its weight is 17.9 kN, its external volume is 1.708 m^3, and its apparent unit weight is 10.5 kN/m^3. Zero to three weight rings and groundwater table depths of 0–2 m were considered. The assumed soil parameters were $\gamma_t = 18$ kN/m^3, $\gamma_{sat} = 19$ kN/m^3, $\gamma_w = 10$ kN/m^3, $K_0 = 0.5$, $\varphi = 30°$, and an interface friction angle of $2\varphi/3$. These are assumed values and were not measured. The soil below the groundwater table was assumed to liquefy to the ratio r_u with pressure profile I. The soil above it was assumed to retain its strength. The friction Q_B acts on the vertical envelope surface

above the groundwater table. The diameter of this surface is 1.6 m over the height of the collar and 1.05 m below it. The weight W_S is that of the unsaturated soil above the cone within the shaft envelope, between the collar base and the groundwater table. Restraint from connected pipes was neglected. The equivalent ratio r_m of the model tests is not used in this calculation. Figure 11 and Table 9 show the factors of safety. Table 10 lists the force components, and Table 11 shows the sensitivity to the assumptions. A calculation sheet with the unrounded components is provided in Additional file 1.

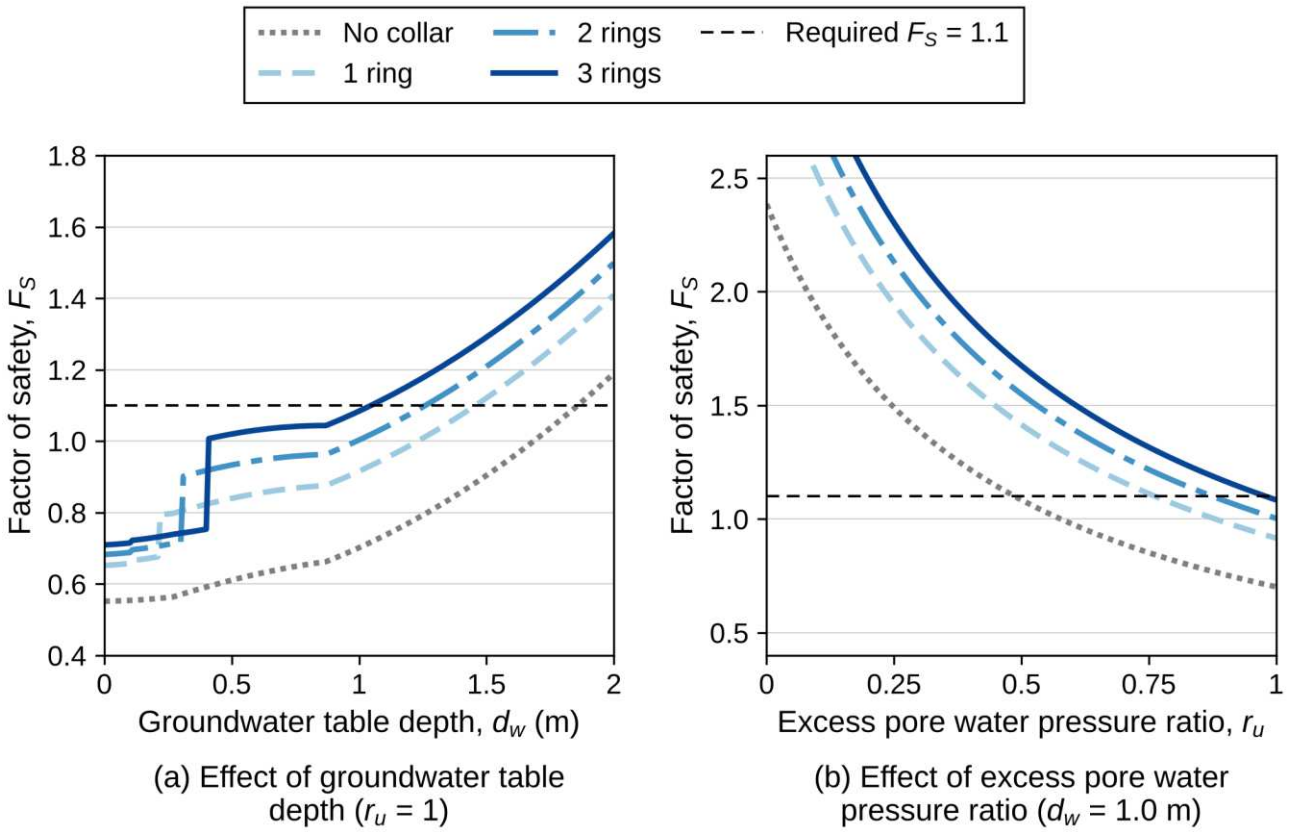

Figure 11. Factor of safety against uplift of the prototype No. 1 manhole with zero to three weight rings.

Table 9. Factor of safety against uplift of the prototype manhole at full liquefaction (r_u = 1, profile I, base assumptions). Threshold depths are rounded to 0.1 m.

Groundwater table depth, d_w (m)	No collar	1 ring (7.39 kN)	2 rings (10.50 kN)	3 rings (13.61 kN)
0	0.55	0.66	0.69	0.72
0.5	0.67	0.86	0.94	1.02
1.0	0.76	0.94	1.01	1.09
1.5	0.96	1.14	1.22	1.30
2.0	1.25	1.43	1.51	1.59
Minimum d_w for $F_S \geq 1.0$ (m)	1.6	1.2	1.0	0.4
Minimum d_w for $F_S \geq 1.1$ (m)	1.8	1.4	1.2	1.0
Critical ratio, $r_{u,cr}$, at d_w = 1.0 m	0.66	0.91	1.02	1.13

Table 10. Force components (kN) for the prototype manhole without a collar and with three rings ($r_u = 1$, profile I, base assumptions). $F_S = (W_M + W_W + W_S + Q_B)/(U_S + U_D)$.

d_w (m)	Collar	W_M	W_W	W_S	Q_B	U_S	U_D	F_S
0	None	17.90	0.00	0.00	0.00	17.08	15.37	0.55
0	3 rings	17.90	13.61	0.00	0.00	23.11	20.80	0.72
0.5	None	17.90	0.00	2.80	1.35	14.31	18.71	0.67
0.5	3 rings	17.90	13.61	0.39	1.83	14.31	18.71	1.02
1.0	None	17.90	0.00	3.54	5.40	10.39	24.94	0.76
1.0	3 rings	17.90	13.61	1.14	5.88	10.39	24.94	1.09
1.5	None	17.90	0.00	3.54	12.16	6.06	28.83	0.96
1.5	3 rings	17.90	13.61	1.14	12.63	6.06	28.83	1.30
2.0	None	17.90	0.00	3.54	21.61	1.73	32.73	1.25
2.0	3 rings	17.90	13.61	1.14	22.09	1.73	32.73	1.59

Table 11. Sensitivity of the calculated factor of safety of the prototype manhole to the assumptions ($r_u = 1$). One assumption is changed at a time.

Assumption	F_S, no collar, d_w = 1.0 m	F_S, 3 rings, d_w = 1.0 m	F_S, 3 rings, d_w = 0.5 m	Minimum d_w for $F_S \geq 1.1$, 3 rings (m)
Base assumptions (profile I)	0.76	1.09	1.02	1.0
No wall friction ($Q_B = 0$)	0.61	0.92	0.97	not reached
$K_0 = 0.4$	0.73	1.06	1.01	1.2
$K_0 = 0.6$	0.79	1.12	1.03	0.9
Interface friction angle of $\varphi/2$	0.72	1.05	1.01	1.2
$\gamma_{sat} = 18$ kN/m^3	0.78	1.12	1.07	0.9
$\gamma_{sat} = 20$ kN/m^3	0.74	1.06	0.98	1.1
$\gamma_t = 17$ kN/m^3	0.76	1.11	1.03	1.0
Profile II (zero excess pressure at the groundwater table)	1.36	1.95	1.24	0.4
Profile II without wall friction	1.09	1.65	1.17	0.4

The following results apply to this configuration and to these assumptions.

First, the manhole without a collar is light. With the groundwater table at the ground surface, its critical excess pore water pressure ratio is 0.05. With profile I and the assumed friction, its factor of safety at full liquefaction reaches 1.1 only when the groundwater table is deeper than about 1.8 m, which is close to its base.

Second, the calculated benefit of the collar depends strongly on whether the collar is submerged. Table 10 gives the terms of the incremental balance of Section 2.2. With the groundwater table at the ground surface, three rings add 13.61 kN of weight. They also add 0.60 m^3 of displaced volume. The pore water pressure force on this volume is 11.46 kN, of which 6.03 kN is hydrostatic and 5.43 kN is excess. The net gain is 2.2 kN, or 16% of the nominal weight. The factor of safety increases only from 0.55 to 0.72. With a groundwater table depth of 1.0 m, the collar is above the groundwater table, and the pore water pressure forces are unchanged. The collar adds 13.61 kN of weight and 0.48 kN of friction on its wider surface. It replaces soil above the cone that weighed 2.40 kN. The net gain is 11.68 kN, and the factor of safety increases from 0.76 to 1.09. The increase therefore does not follow from the added weight alone.

Third, the factor of safety with three rings changes abruptly when the groundwater table passes the collar base at a depth of 0.41 m. Under profile I, it is 0.76 for a groundwater table depth of 0.409 m and 1.01 for a depth of 0.411 m. This jump is a mathematical discontinuity of the idealization. The submerged collar volume changes the buoyancy gradually and causes only a change in slope. The jump comes from the surface term of Eq. (3). This term is proportional to the cross-sectional area at the groundwater table, which changes from 2.01 m^2 within the collar to 0.60 m^2 below it. Under profile II, which has no surface term, the factor of safety is continuous (1.16 at both depths). The apparent threshold at the collar base is therefore a feature of profile I and not a verified physical boundary.

Fourth, the threshold depths are sensitive to the assumptions (Table 11). With the base assumptions, three rings give $F_S \geq 1.1$ at full liquefaction for groundwater table depths greater than about 1.0 m. The corresponding depth without the collar is about 1.8 m. When K_0, the interface friction angle, and the unit weights are varied as in Table 11, the depth for three rings varies between about 0.9 and 1.2 m. Without wall friction, the factor of safety with three rings is below unity at all groundwater table depths under profile I. Under profile II, the factors of safety are much higher. The pressure profile at the groundwater table and the wall friction therefore have a larger influence than the number of rings. The threshold depths are approximate values for the selected configuration, with a precision of 0.1–0.2 m at best. For a groundwater table depth of 1.0 m, the critical ratio increases from 0.66 without rings to 0.91, 1.02, and 1.13 with one, two, and three rings. The critical ratios and the factors of safety in Table 9 were calculated from the same unrounded components. A critical ratio of 1.02 corresponds to a factor of safety of 1.01 at $r_u = 1$. Values this close to unity do not distinguish a stable state from an unstable state.

Fifth, the conventional base-area calculation was compared with Eqs. (1)–(4) for the manhole without a collar. For a groundwater table depth of 1.0 m, the cone lies above the groundwater table, and the two calculations give the same factor of safety (0.76). For a groundwater table at the ground surface and $r_u = 1$, the base-area calculation gives 0.60, and the integration gives 0.55. The net vertical force is the same in both calculations. The base-area calculation adds the total weight of the saturated soil above the cone to the resistance. The integration subtracts the equal downward pressure force from the uplift force. The ratio differs, but the condition $F_S = 1$ is identical. For $r_u = 0.5$, the values are 0.78 and 0.72. The integration then also neglects the effective weight of the soil above the cone, and it gives 0.76 if this weight is included. The two formulations are therefore equivalent when all forces are included consistently. The integration makes the terms explicit, which is useful when a collar is added.

The factor of safety for a given number of rings, groundwater table depth, and excess pore water pressure ratio can be read from Fig. 11. The figure applies only to the selected manhole and to the base assumptions. The floating-equilibrium displacement of Eq. (7) was not evaluated for the prototype. Its assumptions are more restrictive than the groundwater conditions considered here, and displacements cannot be scaled from the 1-g tests (Section 3.5).

6. DISCUSSION

6.1 Interpretation of the Observed Response

The experimental observation is clear. Without the collar, the model was uplifted by 8–12% of its height. With the collar, it showed no measurable uplift at any of the three shaking levels in the same deposit. Under the assumption of full liquefaction, the change in apparent unit weight does not explain this result. The collar increased the apparent unit weight by only 6%. Both models remained much lighter than the liquefied soil, and a heavy-fluid calculation predicts uplift of both.

One interpretation is consistent with the measurements. In this interpretation, uplift in these tests was governed by a small force margin and not by the unit weight contrast itself. An equivalent excess pore water pressure ratio of about 0.5 is compatible with the displacement of the unweighted model. The unweighted model has a critical ratio of 0.38. Its calculated net uplift force at a ratio of 0.5 is about 0.2 N, or 8% of its weight. The weighted model has a critical ratio of 0.47–0.63 in the two limiting scenarios. A change of 0.1–0.25 in the critical ratio would then be sufficient to move the model from the unstable side of the threshold to its vicinity or to the stable side. This interpretation is not unique. The collar changed the weight, the buoyancy, and the geometry near the ground surface at the same time. A wider collar may also change the local drainage and add resistance in the shallow soil. The individual contributions of mass, geometry, and local drainage cannot be separated with the present tests. In addition, the calculated factors of safety of the weighted model are close to unity and are sensitive to the modeling assumptions.

If the force margin is small, moderate differences in groundwater table depth, backfill density, or pipe restraint could determine whether a manhole is uplifted. This would agree with the wide variation in uplift displacement among nominally similar manholes reported after earthquakes (Yasuda and Kiku 2006; Tobita et al. 2009). However, the present tests do not examine this variation. Whether existing manholes are generally close to

the stability threshold depends on their weight, geometry, and groundwater conditions. This question requires a representative dataset and is left for future assessment.

6.2 Implications for Disaster Mitigation and Design

From a disaster-mitigation perspective, the retrofit addresses one damage mode, the uplift of the manhole itself, by a shallow intervention that could be applied to many existing manholes within short road closures. Its value for a mitigation program depends on whether this damage mode is the one that governs the loss of function at a given site. The conventional design check (Japan Sewage Works Association 2006; Japan Road Association 1986) computes the pore water pressure forces on the base area and assumes full liquefaction below the groundwater table. The present calculations suggest three points for the selected prototype configuration. They are observations on the calculation and not validated design rules.

(1) *Account for the buoyancy of the collar and for the soil that it replaces.* The added weight should enter the factor of safety through the incremental balance of Section 2.2 and not as the nominal weight. If the collar lies above the groundwater table, its nominal weight is reduced only by the weight of the replaced soil. If the design high groundwater level reaches the collar, most of the calculated benefit is lost. Keeping the collar above the groundwater table preserves its dead-weight contribution. It does not by itself ensure an adequate factor of safety. The factor of safety also depends on the groundwater table depth, the manhole geometry, the collar weight, and the assumed resistance. The groundwater condition must be checked for each site and for the seasonal high groundwater level.

(2) *Treat the groundwater table depth and the pressure profile as primary variables.* For the selected manhole and the base assumptions, three rings give $F_S \geq 1.1$ at full liquefaction when the groundwater table is deeper than about 1.0 m. The criterion $F_S \geq 1.1$ is the value specified for the uplift of buried structures in the design guideline for common utility ducts (Japan Road Association 1986). The same criterion is applied here to the retrofitted manhole, and its applicability is assumed. The threshold depth changes by a few tenths of a meter with the assumed friction and unit weights, and much more with the pressure profile (Table 11). A parametric check is therefore more informative than a single threshold.

(3) *Keep the design pressure assumption separate from the back-analysis.* The equivalent ratio of about 0.5 was obtained from three small-scale tests and from the same records that it is used to interpret. It is not a design reduction factor, and it does not demonstrate an additional safety margin. The prototype examples therefore

retain the full-liquefaction assumption. The pressure that acts on a manhole during shaking is the quantity that further study should address.

The retrofit does not reduce the settlement of the surrounding ground. In loose backfill, a weighted manhole may therefore still protrude above a settled road surface after an earthquake, and the resulting step may still hinder traffic. In the tests, the estimated protrusion of the weighted model was about half of that of the unweighted model. Pipe connections were not modeled, and the continuity of wastewater service was not examined. Where the backfill is very loose over a large depth, a combination with partial replacement or drainage of the upper backfill (Kang et al. 2013; Orense et al. 2003; Otsubo et al. 2016b) may be considered. Such combinations were not studied here.

6.3 Screening and Prioritization for Pre-Earthquake Retrofit

The results can be applied to existing networks through a screening procedure rather than a uniform specification. The procedure proposed here has three steps. It combines the consequence of failure at each manhole, the groundwater and backfill conditions that control the calculated benefit of the collar, and the functional performance that the retrofit is expected to secure. The procedure uses the prototype calculation of Section 5.4 and the qualitative findings of the tests. It does not use the equivalent ratio r_m or any displacement measured at model scale.

- *Step 1: Prioritization by consequence.* Manholes are ranked by the consequence of their failure for emergency response and for wastewater service.
- *Step 2: Screening by groundwater and backfill conditions.* The seasonal high groundwater table depth and the condition of the backfill are used to determine whether the collar can provide the required resistance.
- *Step 3: Verification of the functional performance.* The residual road surface step and the pipe connections are checked against the function that the manhole must retain after an earthquake.

In Step 1, the network is divided by the function that each manhole supports immediately after an earthquake. Manholes beneath designated emergency transport routes govern the access of rescue, firefighting, and supply vehicles. Manholes on sewers that serve evacuation centers, hospitals, and disaster management facilities govern the continuity of sanitation at the locations where it is needed most. Manholes on trunk sewers govern the service of large areas, because damage at one location can interrupt the flow from all upstream branches. Manholes beneath local streets with alternative routes form a lower priority class. This classification

follows from the consequences described in Section 1.1. The ranking criteria and weights are a matter for the road and sewer administrators and are not proposed here.

In Step 2, the groundwater table depth is the primary variable, because it determines whether the collar is submerged. In the calculation of Section 5.4, a submerged collar retained only 16% of its nominal weight as a net gain, whereas a collar above the groundwater table retained most of its dead-weight contribution. The relevant depth is the seasonal high groundwater level and not a single measurement, since an earthquake may occur at any time of year. The calculated factor of safety for this depth is then compared with the criterion $F_S \geq 1.1$ (Japan Road Association 1986). Because values close to the criterion do not distinguish a stable state from an unstable state (Section 5.4), a marginal band is introduced. In the example below, a configuration is classified as marginal if its factor of safety under the base assumptions lies between 1.0 and 1.2, or if it falls below 1.0 for any of the variations in Table 11. The width of this band is a choice made for illustration and has not been calibrated. The backfill condition is used qualitatively. Loose sandy backfill below the groundwater table justifies the assumption of full liquefaction, whereas well-compacted or improved backfill may justify a separate liquefaction assessment before the retrofit is selected.

In Step 3, the expected performance is checked against the function identified in Step 1. The tests show that suppression of uplift and limitation of the road surface step are different objectives. The weighted model was not uplifted, but its estimated protrusion above the settled ground surface was about half of that of the unweighted model (Section 4.4). For a manhole on an emergency transport route, the reconsolidation settlement of the surrounding backfill should therefore be estimated, for example from the volumetric strain after liquefaction (Ishihara and Yoshimine 1992), and compared with the step that the road administrator can tolerate. For a manhole that must maintain wastewater service, the capacity of the pipe connections to accommodate the relative displacement between a stationary manhole and the settling ground should be examined. Neither check was addressed in this study. Where either check is not satisfied, the collar can be combined with partial replacement or drainage of the upper backfill, or another measure can be selected.

Table 12 illustrates the procedure for five hypothetical manholes. All five are assumed to be the standard No. 1 manhole of Section 5.4, with full liquefaction ($r_u = 1$), pressure profile I, and the base assumptions. They differ only in their setting and in the seasonal high groundwater table depth. The factors of safety are taken directly from Table 9. The settings are invented for illustration and do not represent surveyed sites.

Table 12. Illustrative screening of five hypothetical No. 1 manholes (r_u = 1, profile I, base assumptions). The factors of safety are taken from Table 9. Values between 1.0 and 1.2 are classified as marginal.

Manhole	Setting and consequence of failure	Seasonal high groundwater table depth (m)	Factor of safety: no collar / 1 / 2 / 3 rings	Screening outcome
M1	Designated emergency transport route; sewer serving an evacuation center; loose sandy backfill	1.5	0.96 / 1.14 / 1.22 / 1.30	Collar applicable in the calculation; three rings selected, because one ring lies in the marginal band; proceed to Step 3
M2	Designated emergency transport route; loose sandy backfill	1.0	0.76 / 0.94 / 1.01 / 1.09	Marginal; 0.92 with three rings and no wall friction (Table 11); refine the groundwater and backfill data or combine with a backfill measure
M3	Road to a hospital; loose sandy backfill	0.5	0.67 / 0.86 / 0.94 / 1.02	Collar above the groundwater table but insufficient alone; backfill replacement or drainage required
M4	Trunk sewer in reclaimed land; loose sandy backfill	0	0.55 / 0.66 / 0.69 / 0.72	Collar submerged; not suitable as a stand-alone measure
M5	Local street with alternative routes; loose sandy backfill	2.0	1.25 / 1.43 / 1.51 / 1.59	Criterion met without a collar in the calculation; low priority for this retrofit

The example shows how the outcome changes with the groundwater condition. Manhole M1 is the only high-priority case in which the collar satisfies the criterion with a clear margin. Even in this case, Step 3 remains necessary, because the collar does not limit the settlement of the surrounding backfill. The sensitivity analysis of Table 11 was carried out only for groundwater table depths of 0.5 and 1.0 m, so that the margin of M1 under other assumptions has not been calculated. Manhole M2 illustrates the marginal band. Three rings give 1.09 under the base assumptions, but 0.92 without wall friction. The decision for this manhole depends on whether the wall friction above the groundwater table can be relied on during shaking, which the present study cannot establish. Manhole M3 shows that a collar above the groundwater table is not sufficient by itself when the groundwater table is shallow. Manhole M4 represents the reclaimed land in which extensive uplift occurred in 2011 (Tokimatsu et al. 2012; MLIT 2011; Chian and Tokimatsu 2012). There the collar is submerged, its calculated benefit is small, and measures that address the backfill or the pore water pressure are required. Manhole M5 already satisfies the criterion in the calculation and has a low consequence class. Its priority for this retrofit is therefore low, although the settlement of the backfill may still require attention.

Two points qualify this example. First, all values refer to one manhole type and to assumed soil parameters, and the factors of safety under profile II are much higher (Table 11). The classification of a given site can therefore change with the pressure assumption, and a site-specific calculation is required. Second, the procedure has not been tested against field performance. Its value lies in making explicit which conditions a weight collar can address and which it cannot. Whether the thresholds used here are appropriate should be examined with post-earthquake damage records and with analyses at prototype stress levels.

6.4 Limitations and Future Work

The following limitations qualify specific conclusions. Each item states what it affects.

- *Low-stress 1-g modeling.* The tests were conducted at 1 g with effective stresses below 2 kPa. Sand at such stresses is more dilative (Bolton 1986), and more permeable relative to its stiffness (Haigh et al. 2012), than sand at field stresses. This affects the pressure buildup, the drainage time, the equivalent ratio r_m, and the time constants. None of these values can be transferred to a prototype.
- *Imperfect similitude.* The models reproduce the external shape of the prototype but not its mass, height, or buoyancy (Table 5). This affects any direct comparison between the models and the prototype. The prototype calculation of Section 5.4 does not use the test results.
- *Unresolved cyclic pore water pressure.* The stored sampling interval did not resolve the 3 Hz component. The records contain an undiagnosed periodic disturbance. The transducers were free to move, and their accuracy is not documented. This affects the magnitude of the apparent r_u, including the values above unity, and the timing of the pressure buildup in Case A-50. The association between pressure buildup and uplift in Cases A-100 and A-150 is insensitive to the smoothing window.
- *Unknown local pressure distribution.* The pore water pressure was measured at two free-field points below the level of the collar. No pressure was measured on the models or at shallow depth. The saturation of the deposit was not checked independently. This affects the choice between cases A and B, the meaning of r_m, and the explanation of the response of the weighted model.
- *Confounding of geometry and mass.* The collar changed the mass and the external geometry together. This affects the attribution of the observed response. The tests show only the response of the complete collar configuration.
- *Omitted pipes and trench.* The models were not connected to pipes, and the deposit was uniform. In the field, a trench of limited width lies within native ground, and an unsaturated layer lies above the groundwater table (Yasuda and Kiku 2006; Tobita et al. 2011). This affects the applicability to field conditions and excludes any statement about pipe connections. The direction of the combined effect is unresolved.
- *Input motion, timing, and replication.* The input motion was sinusoidal, unidirectional, and long. The acceleration was not recorded, and the start and end of shaking were inferred. Each case was tested once, and the clearances of the models were not recorded. This affects the statements on the timing of uplift relative to shaking, the comparison among the three amplitudes, and the repeatability of all results.

- *Simplified analysis.* The limit equilibrium model is static. It represents the pore water pressure field by a single ratio and an idealized profile, and the wall friction parameters are assumed. The first-order uplift model is phenomenological. This affects the factors of safety close to unity, the threshold depths of Section 5.4, and the fitted parameters. Structural verification of the collar connection was not performed.

Future work should address these limitations. Pressure measurements on the base and the collar, layered ground with a lowered groundwater table, irregular input motions, tests at prototype stress levels, and coupled effective stress analyses would be required to convert the present observations into design guidance. Post-earthquake surveys that compare retrofitted and unretrofitted manholes in the same area would provide the field evidence needed to evaluate the method as a disaster-mitigation measure.

7. CONCLUSIONS

A retrofit against liquefaction-induced uplift of existing manholes was examined as a pre-earthquake mitigation measure for sewer and road networks. In this retrofit, a weight collar of precast weight rings and non-shrink mortar is installed around the manhole top from the road surface, within a depth of 425 mm. Paired 1-g shaking table tests on small models and a limit equilibrium calculation were conducted. The conclusions are restricted to the tested configuration and conditions. They are ordered from observation to interpretation.

(1) *Observation.* The tests were conducted in nominally saturated sand with a relative density of 38–40% and the groundwater table at the ground surface. Under sinusoidal shaking with nominal amplitudes of 0.5, 1.0, and 1.5 m/s^2, the unweighted model was uplifted by 9.6, 10.1, and 14.0 mm (8.2–11.9% of its height). The model with the collar, in the same deposit, showed no measurable uplift in any test. It settled by 0.4–1.0 mm.

(2) *Observation.* Uplift of the unweighted model followed a substantial buildup of excess pore water pressure. At 1.0 and 1.5 m/s^2, uplift began at about the time when the smoothed pressure 80 mm below the base reached the estimated initial vertical effective stress. At 0.5 m/s^2, it began at an apparent ratio of 0.4–0.5. The magnitudes of the recorded pressures are uncertain, and the pressure around the models was not measured. Most of the uplift accumulated during shaking.

(3) *Interpretation.* The force-balance calculation is consistent with a stabilizing contribution of the collar. The critical excess pore water pressure ratio is 0.38 for the unweighted model and 0.47–0.63 for the weighted

model. However, the collar changed the mass and the geometry together. The individual effects of mass, geometry, and local drainage cannot be separated.

(4) *Back-analysis.* An equivalent excess pore water pressure ratio of about 0.45–0.55 was back-calculated from the displacement of the unweighted model. It is conditional on the assumed force balance and is not a measured pressure ratio. Over this range, the calculated factor of safety of the weighted model is 0.95–1.09; with the case-specific ratios, it is 0.97–1.09. These values are close to unity and are a consistency check, not an independent validation. The uplift time histories are described by a phenomenological first-order model with time constants of 15–24 s at model scale.

(5) *Prototype illustration.* For the standard No. 1 manhole with the assumed pressure profile and wall friction, three rings (13.6 kN) increase the calculated factor of safety at full liquefaction from 0.76 to 1.09 for a groundwater table depth of 1.0 m. With the groundwater table at the ground surface, the increase is only from 0.55 to 0.72, because the submerged collar displaces liquefied soil. Keeping the collar above the groundwater table preserves its dead-weight contribution, but it does not by itself ensure adequate resistance. The calculated values depend strongly on the assumed pressure profile and wall friction. They do not establish a generally applicable design threshold.

(6) *Functional implication.* Suppression of absolute uplift does not eliminate protrusion caused by ground settlement. The estimated protrusion above the mean settled ground surface was 10–13 mm for the weighted model and 21–27 mm for the unweighted model. For post-earthquake road access, the step between the manhole and the settled road surface, and not the absolute uplift alone, is the relevant measure. The integrity of connected pipes, and hence the continuity of wastewater service, and the structural adequacy of the collar connection were not examined.

The tests provide exploratory evidence that the tested collar configuration suppressed measurable absolute uplift under the reported small-scale conditions and roughly halved the estimated protrusion. The simplified analysis offers one consistent interpretation of this result and identifies the groundwater table depth as a primary screening variable for retrofit sites. Prototype performance, the residual road surface step, pipe connections, and design thresholds remain to be established at prototype stress levels, in trench-type ground, by coupled effective stress analysis, and by post-earthquake field observation.

NOTATION

Symbol	Meaning
$A(d_w)$	Horizontal cross-sectional area of the structure at the groundwater table
A_n	Cross-sectional area of the manhole neck
c	Resistance coefficient of liquefied soil against uplift
D_r	Relative density
d_w	Groundwater table depth
F_S	Factor of safety against uplift
h	Height of the manhole
k	Buoyant stiffness
Q_B	Frictional resistance on the wall above the groundwater table
r_u, $r_{u,cr}$, r_m	Excess pore water pressure ratio; critical value; equivalent back-calculated value
t, t_0	Logger time; start of uplift
U_S, U_D	Hydrostatic and excess pore water pressure forces
V, V_c, V_s	External volume of the structure; of the collar; below the original ground surface after uplift
W_M, W_W, W_S	Weight of manhole; weight of collar; weight of unsaturated soil above the cone
γ_m	Apparent unit weight of the structure
γ_t, γ_{sat}, γ', γ_w	Total, saturated, and buoyant unit weights of soil; unit weight of water
δ, δ_∞, δ_f	Uplift displacement; asymptotic value; floating-equilibrium value
Δu	Excess pore water pressure
λ	Geometric scale factor (prototype/model)
σ'_{v0}	Initial vertical effective stress
τ	Time constant of uplift

Declarations

Ethics approval and consent to participate. Not applicable.

Consent for publication. Not applicable.

Availability of data and materials. The datasets supporting the conclusions of this article are included within the article and its additional file (Additional file 1). Additional file 1 contains the displacement and pore water pressure records, the processing parameters, the geometric inputs, and the calculation tables for the model manholes and the prototype. The acceleration of the shaking table was not recorded and is therefore not available.

Competing interests. The authors declare that they have no competing interests.

Funding. Not applicable.

Authors' contributions. KNCK and DF prepared the model ground, conducted the shaking table tests, and processed the test records. SI conceived and supervised the study, developed the analytical interpretation, and wrote the manuscript. All authors read and approved the final manuscript.

Acknowledgements. Not applicable.

Supplementary Information

Additional file 1 (.xlsx). Test records and calculation sheets. Displacement and pore water pressure records of Cases A-50, A-100, and A-150, the processing parameters, the geometric inputs, and the calculation tables for the model manholes and the prototype manhole (Sections 3–5).

REFERENCES

Azadi M, Mir Mohammad Hosseini SM (2010) The uplifting behavior of shallow tunnels within the liquefiable soils under cyclic loadings. Tunn Undergr Space Technol 25(2):158–167. https://doi.org/10.1016/j.tust.2009.10.004

Bhattacharya S, Hyodo M, Goda K, Tazoh T, Taylor CA (2011) Liquefaction of soil in the Tokyo Bay area from the 2011 Tohoku (Japan) earthquake. Soil Dyn Earthq Eng 31(11):1618–1628. https://doi.org/10.1016/j.soildyn.2011.06.006

Bolton MD (1986) The strength and dilatancy of sands. Géotechnique 36(1):65–78. https://doi.org/10.1680/geot.1986.36.1.65

Chian SC, Madabhushi SPG (2012) Effect of buried depth and diameter on uplift of underground structures in liquefied soils. Soil Dyn Earthq Eng 41:181–190. https://doi.org/10.1016/j.soildyn.2012.05.020

Chian SC, Tokimatsu K (2012) Floatation of underground structures during the Mw 9.0 Tōhoku earthquake of 11th March 2011. In: Proceedings of the 15th World Conference on Earthquake Engineering, Lisbon

Chian SC, Tokimatsu K, Madabhushi SPG (2014) Soil liquefaction–induced uplift of underground structures: physical and numerical modeling. J Geotech Geoenviron Eng 140(10):04014057. https://doi.org/10.1061/(ASCE)GT.1943-5606.0001159

Chou JC, Kutter BL, Travasarou T, Chacko JM (2011) Centrifuge modeling of seismically induced uplift for the BART Transbay Tube. J Geotech Geoenviron Eng 137(8):754–765. https://doi.org/10.1061/(ASCE)GT.1943-5606.0000489

Cubrinovski M, Bradley B, Wotherspoon L, Green R, Bray J, Wood C, Pender M, Allen J, Bradshaw A, Rix G, Taylor M, Robinson K, Henderson D, Giorgini S, Ma K, Winkley A, Zupan J, O'Rourke T, DePascale G, Wells D (2011) Geotechnical aspects of the 22 February 2011 Christchurch earthquake. Bull N Z Soc Earthq Eng 44(4):205–226. https://doi.org/10.5459/bnzsee.44.4.205-226

1082 Haigh SK, Eadington J, Madabhushi SPG (2012) Permeability and stiffness of sands at very low effective
1083 stresses. Géotechnique 62(1):69–75. https://doi.org/10.1680/geot.10.P.035
1084 Hwang JI, Kim CY, Chung CK, Kim MM (2006) Viscous fluid characteristics of liquefied soils and behavior of
1085 piles subjected to flow of liquefied soils. Soil Dyn Earthq Eng 26(2–4):313–323.
1086 https://doi.org/10.1016/j.soildyn.2005.02.020
1087 Iai S (1989) Similitude for shaking table tests on soil-structure-fluid model in 1g gravitational field. Soils Found
1088 29(1):105–118. https://doi.org/10.3208/sandf1972.29.105
1089 Idriss IM, Boulanger RW (2008) Soil liquefaction during earthquakes. Monograph MNO-12. Earthquake
1090 Engineering Research Institute, Oakland, CA
1091 Ishihara K (1993) Liquefaction and flow failure during earthquakes. Géotechnique 43(3):351–451.
1092 https://doi.org/10.1680/geot.1993.43.3.351
1093 Ishihara K, Yoshimine M (1992) Evaluation of settlements in sand deposits following liquefaction during
1094 earthquakes. Soils Found 32(1):173–188. https://doi.org/10.3208/sandf1972.32.173
1095 Japan Road Association (1986) Design guidelines for common utility ducts. Japan Road Association, Tokyo (in
1096 Japanese)
1097 Japan Sewage Works Association (2005) Precast reinforced concrete manholes for sewerage, JSWAS A-11. Japan
1098 Sewage Works Association, Tokyo (in Japanese)
1099 Japan Sewage Works Association (2006) Guidelines and commentary for seismic countermeasures of sewerage
1100 facilities. Japan Sewage Works Association, Tokyo (in Japanese)
1101 Japanese Geotechnical Society (2014) Report on proficiency testing for laboratory tests of geomaterials. Japanese
1102 Geotechnical Society, Tokyo (in Japanese)
1103 Kang GC, Tobita T, Iai S (2014) Seismic simulation of liquefaction-induced uplift behavior of a hollow cylinder
1104 structure buried in shallow ground. Soil Dyn Earthq Eng 64:85–94.
1105 https://doi.org/10.1016/j.soildyn.2014.05.006
1106 Kang GC, Tobita T, Iai S, Ge L (2013) Centrifuge modeling and mitigation of manhole uplift due to liquefaction.
1107 J Geotech Geoenviron Eng 139(3):458–469. https://doi.org/10.1061/(ASCE)GT.1943-5606.0000769
1108 Koseki J, Matsuo O, Koga Y (1997a) Uplift behavior of underground structures caused by liquefaction of
1109 surrounding soil during earthquake. Soils Found 37(1):97–108. https://doi.org/10.3208/sandf.37.97
1110 Koseki J, Matsuo O, Ninomiya Y, Yoshida T (1997b) Uplift of sewer manholes during the 1993 Kushiro-Oki
1111 earthquake. Soils Found 37(1):109–121. https://doi.org/10.3208/sandf.37.109

Koseki J, Matsuo O, Tanaka S (1998) Uplift of sewer pipes caused by earthquake-induced liquefaction of surrounding soil. Soils Found 38(3):75–87. https://doi.org/10.3208/sandf.38.3_75

Ling HI, Mohri Y, Kawabata T, Liu H, Burke C, Sun L (2003) Centrifugal modeling of seismic behavior of large-diameter pipe in liquefiable soil. J Geotech Geoenviron Eng 129(12):1092–1101. https://doi.org/10.1061/(ASCE)1090-0241(2003)129:12(1092)

Liu H, Song E (2005) Seismic response of large underground structures in liquefiable soils subjected to horizontal and vertical earthquake excitations. Comput Geotech 32(4):223–244. https://doi.org/10.1016/j.compgeo.2005.02.002

Mahmoud AO, Hussien MN, Karray M, Chekired M, Bessette C, Jinga L (2020) Mitigation of liquefaction-induced uplift of underground structures. Comput Geotech 125:103663. https://doi.org/10.1016/j.compgeo.2020.103663

Miyajima M, Yoshida M, Serikawa Y (2024) Quick report of preliminary reconnaissance of the 2024 Noto-hanto earthquake in Japan. Earthquake Engineering Committee, Japan Society of Civil Engineers. https://committees.jsce.or.jp/eec205/system/files/Quick%20report%20of%20preliminary%20investigation.pdf. Accessed 16 Nov 2026

MLIT (Ministry of Land, Infrastructure, Transport and Tourism) (2011) Summary of damage to sewerage facilities in the Great East Japan Earthquake. MLIT, Tokyo (in Japanese)

Nakao K, Yamaguchi H, Hoshino S, Inazumi S (2022) Applicability of weighting method as measure for existing manholes against uplifting during liquefaction. Appl Sci 12(8):3818. https://doi.org/10.3390/app12083818

Nokande S, Haddad A, Jafarian Y (2023) Shaking table test on mitigation of liquefaction-induced tunnel uplift by helical pile. Int J Geomech 23(1):04022243. https://doi.org/10.1061/(ASCE)GM.1943-5622.0002607

Orense RP, Morimoto I, Yamamoto Y, Yumiyama T, Yamamoto H, Sugawara K (2003) Study on wall-type gravel drains as liquefaction countermeasure for underground structures. Soil Dyn Earthq Eng 23(1):19–39. https://doi.org/10.1016/S0267-7261(02)00152-5

Otsubo M, Towhata I, Hayashida T, Shimura M, Uchimura T, Liu B, Taeseri D, Cauvin B, Rattez H (2016a) Shaking table tests on mitigation of liquefaction vulnerability for existing embedded lifelines. Soils Found 56(3):348–364. https://doi.org/10.1016/j.sandf.2016.04.003

Otsubo M, Towhata I, Hayashida T, Liu B, Goto S (2016b) Shaking table tests on liquefaction mitigation of embedded lifelines by backfilling with recycled materials. Soils Found 56(3):365–378. https://doi.org/10.1016/j.sandf.2016.04.004

1142 Sasaki T, Tamura K (2004) Prediction of liquefaction-induced uplift displacement of underground structures. In:
1143 Proceedings of the 36th Joint Meeting of the US–Japan Panel on Wind and Seismic Effects, Gaithersburg,
1144 MD
1145 Scott RF (1986) Solidification and consolidation of a liquefied sand column. Soils Found 26(4):23–31.
1146 https://doi.org/10.3208/sandf1972.26.4_23
1147 Seed HB, Idriss IM (1971) Simplified procedure for evaluating soil liquefaction potential. J Soil Mech Found Div
1148 97(9):1249–1273. https://doi.org/10.1061/JSFEAQ.0001662
1149 Sudevan PB, Boominathan A, Banerjee S (2020) Numerical study of liquefaction-induced uplift of underground
1150 structure. Int J Geomech 20(2):06019020. https://doi.org/10.1061/(ASCE)GM.1943-5622.0001578
1151 Tobita T, Iai S, Kang GC, Konishi Y (2009) Observed damage of wastewater pipelines and estimated manhole
1152 uplifts during the 2004 Niigataken Chuetsu, Japan, earthquake. In: TCLEE 2009: Lifeline Earthquake
1153 Engineering in a Multihazard Environment. ASCE, Reston, VA, pp 1–12.
1154 https://doi.org/10.1061/41050(357)75
1155 Tobita T, Kang GC, Iai S (2011) Centrifuge modeling on manhole uplift in a liquefied trench. Soils Found
1156 51(6):1091–1102. https://doi.org/10.3208/sandf.51.1091
1157 Tobita T, Kang GC, Iai S (2012) Estimation of liquefaction-induced manhole uplift displacements and trench-
1158 backfill settlements. J Geotech Geoenviron Eng 138(4):491–499. https://doi.org/10.1061/(ASCE)GT.1943-
1159 5606.0000615
1160 Tokimatsu K, Tamura S, Suzuki H, Katsumata K (2012) Building damage associated with geotechnical problems
1161 in the 2011 Tohoku Pacific Earthquake. Soils Found 52(5):956–974.
1162 https://doi.org/10.1016/j.sandf.2012.11.014
1163 Towhata I (2008) Geotechnical earthquake engineering. Springer, Berlin. https://doi.org/10.1007/978-3-540-
1164 35783-4
1165 Watanabe K, Sawada R, Koseki J (2016) Uplift mechanism of open-cut tunnel in liquefied ground and simplified
1166 method to evaluate the stability against uplifting. Soils Found 56(3):412–426.
1167 https://doi.org/10.1016/j.sandf.2016.04.008
1168 Yasuda S, Harada K, Ishikawa K, Kanemaru Y (2012) Characteristics of liquefaction in Tokyo Bay area by the
1169 2011 Great East Japan Earthquake. Soils Found 52(5):793–810. https://doi.org/10.1016/j.sandf.2012.11.004
1170 Yasuda S, Kiku H (2006) Uplift of sewage manholes and pipes during the 2004 Niigataken-Chuetsu earthquake.
1171 Soils Found 46(6):885–894. https://doi.org/10.3208/sandf.46.885

1172 Youd TL, Idriss IM, Andrus RD, Arango I, Castro G, Christian JT, Dobry R, Finn WDL, Harder LF Jr, Hynes
1173 ME, Ishihara K, Koester JP, Liao SSC, Marcuson WF III, Martin GR, Mitchell JK, Moriwaki Y, Power MS,
1174 Robertson PK, Seed RB, Stokoe KH II (2001) Liquefaction resistance of soils: summary report from the
1175 1996 NCEER and 1998 NCEER/NSF workshops on evaluation of liquefaction resistance of soils. J Geotech
1176 Geoenviron Eng 127(10):817–833. https://doi.org/10.1061/(ASCE)1090-0241(2001)127:10(817)

Supplementary Files

This is a list of supplementary files associated with this preprint. Click to download.

- SupplementaryDataS1.xlsx